Single-Cell Spatial Proteomics Analyses of Head and Neck Squamous Cell Carcinoma Reveal Tumor Heterogeneity and Immune Architectures Associated with Clinical Outcome

Katie E. Blise[a,b], Shamilene Sivagnanam[b,c], Grace L. Banik[c,d*], Lisa M. Coussens[b,c], and Jeremy Goecks[a,b,**]

[a]Department of Biomedical Engineering, Oregon Health & Science University, Portland, OR USA
[b]The Knight Cancer Institute, Oregon Health & Science University, Portland, OR USA
[c]Department of Cell, Developmental & Cancer Biology, Oregon Health & Science University, Portland, OR USA
[d]Otolaryngology-Head & Neck Surgery, Oregon Health & Science University, Portland, OR USA
*Current affiliation: Division of Otolaryngology, Children's Hospital of Philadelphia, Philadelphia, PA USA
**Corresponding author

Correspondence:
Jeremy Goecks, Ph.D.
Associate Professor, Department of Biomedical Engineering
Oregon Health & Science University
3181 SW Sam Jackson Park Road, Mail Code: KR-COM, Portland, OR 97239
Tel: 503-494-0490, Email: goecksj@ohsu.edu

Running Title: Single-cell spatial analysis of head and neck cancer

Keywords: head and neck squamous cell carcinoma, spatial proteomics, tumor microenvironment, immune compartmentalization, tumor heterogeneity

Funding: KEB acknowledges funding from the National Cancer Institute (NCI) of the National Institutes of Health under award number 5T32CA254888. LMC acknowledges funding from the NCI awards U01CA224012, R01CA223150, R01CA226909, and R21HD099367 and funding from the Brenden-Colson Center for Pancreatic Care at Oregon Health & Science University (OHSU). JG acknowledges funding under award number U24CA231877. LMC and JG acknowledge funding from the OHSU Knight Cancer Institute, NCI award number U2CCA233280, and the Prospect Creek Foundation to the OHSU SMMART (Serial Measurement of Molecular and Architectural Responses to Therapy) Program. The content is solely the responsibility of the authors and does not necessarily represent the official views of the National Institutes of Health, OHSU, or the Knight Cancer Institute.

Conflict of Interests: L.M. Coussens is a paid consultant for Cell Signaling Technologies, AbbVie Inc., and Shasqi Inc., received reagent and/or research support from Plexxikon Inc., Pharmacyclics, Inc., Acerta Pharma, LLC, Deciphera Pharmaceuticals, LLC, Genentech, Inc., Roche Glycart AG, Syndax Pharmaceuticals Inc., Innate Pharma, NanoString Technologies, and Cell Signaling Technologies, is a member of the Scientific Advisory Boards of Syndax Pharmaceuticals, Carisma Therapeutics, Zymeworks, Inc, Verseau Therapeutics, Cytomix Therapeutics, Inc., Hibercell., Inc., Alkermes, Inc., and Kineta Inc, and is a member of the Lustgarten Therapeutics Advisory working group. No potential conflicts of interest were disclosed by the other authors.

Word count, abstract: 180
Word count, main text: 6001
Figure count: 5 main, 3 supplemental
Table count: 3

ABSTRACT

There is increasing evidence that the spatial organization of cells within the tumor-immune microenvironment (TiME) of solid tumors influences survival and response to therapy in numerous cancer types. Here, we report results and demonstrate the applicability of quantitative single-cell spatial proteomics analyses in the TiME of primary and recurrent human papillomavirus (HPV)-negative head and neck squamous cell carcinoma (HNSCC) tumors. Single-cell compositions of a nine patient, primary and recurrent (n=18), HNSCC cohort is presented, followed by deeper investigation into the spatial architecture of the TiME and its relationship with clinical variables and progression free survival (PFS). Multiple spatial algorithms were used to quantify the spatial landscapes of immune cells within TiMEs and demonstrate that neoplastic tumor-immune cell spatial compartmentalization, rather than mixing, is associated with longer PFS. Mesenchymal (αSMA^{+}) cellular neighborhoods describe distinct immune landscapes associated with neoplastic tumor-immune compartmentalization and improved patient outcomes. Results from this investigation are concordant with studies in other tumor types, suggesting that trends in TiME cellular heterogeneity and spatial organization may be shared across cancers and may provide prognostic value in multiple cancer types.

INTRODUCTION

Tumor microenvironments, comprising both neoplastic tumor cells and recruited stromal cells of various lineages, including a diverse assemblage of immune, mesenchymal, and vascular cells, play a key role in both de novo progression of tumors and regulating

83 response to therapies[1-3]. Numerous studies have reported that, in addition to the types
84 and quantities of cells present in the tumor immune-microenvironment (TiME), the
85 spatial organization of the TiME is prognostic for survival and response to therapy in
86 multiple cancer types[4-13]. Metrics that quantify this spatial organization can range from
87 simple density ratios within specific tumor regions[14], such as the Immunoscore[15], a now
88 commonly used biomarker for colorectal tumor staging, to more complex measures that
89 account for the precise locations of specific cells relative to other cells, such as mixing
90 scores[4] and cellular neighborhood measures[7]. These more advanced spatial
91 quantifications are a result of emerging single-cell multiplex tissue imaging
92 modalities[4,6,7,16-18], which provide detailed phenotypic and effector proteomic markers
93 for each cell, while maintaining the spatial architecture of the tissue assayed. Knowing
94 the precise locations of cells in the TiME enables a deeper understanding of how cells
95 interact within the tumor, as both direct and indirect cell signaling mechanisms require
96 cells to be near, if not directly adjacent to one another[19]. This understanding can aid
97 treatment decisions, as many therapies require spatial proximity of specific cell types for
98 efficacy[10]. Given that single-cell imaging technologies are still relatively new, there is
99 much to be discovered regarding how the spatial organization of cells within the TiME
100 relates to clinical outcome and may be used for patient stratification decisions for
101 therapy.
102
103 Head and neck squamous cell carcinoma (HNSCC) is the sixth leading form of cancer
104 worldwide[20], and it accounts for more than 10,000 deaths per year in the US alone[21].
105 While patients harboring human papillomavirus (HPV) within neoplastic cells tend to

106 exhibit a better prognosis, their HPV-negative [HPV(-)] counterparts typically exhibit T
107 cell suppressive TiMEs and have a significantly greater risk of recurrence and shorter 3-
108 year survival[22-24]. There is a critical need to improve understanding of HNSCC TiMEs to
109 enable better patient stratification for therapy, as well as identify new targets that could
110 be leveraged for therapeutic intervention to improve outcome, particularly for patients
111 with HPV(-) tumors who currently lack promising therapeutic options. We previously
112 developed a multiplex immunohistochemistry (mIHC) imaging platform to aid studies
113 investigating the immune contexture of solid tumors and their response to therapies at
114 the single-cell level[16,17]. Using a sequential antibody staining protocol, detection of 12-
115 30 proteins can be enumerated at single-cell resolution across a single formalin-fixed
116 paraffin-embedded (FFPE) tissue section. This enables single-cell phenotyping of
117 discrete leukocyte lineages, and importantly, reveals their spatial relationships with
118 other cells in the tissue section. Utilizing this mIHC approach on a small cohort of
119 eighteen HPV(-) primary and matched recurrent HNSCC tumor samples collected from
120 nine patients, we previously reported immune contextures associated with disease
121 recurrence, most notably that myeloid inflamed profiles in primary tumors exhibited
122 shorter progression free survival (PFS) compared to lymphoid inflamed profiles[16,17].
123
124 In this study, we have significantly extended our prior analysis of this cohort, focusing
125 on tumor heterogeneity and compositional changes from primary to recurrent tumors, in
126 addition to using multiple spatial algorithms to quantify the spatial organization of the
127 TiMEs. We then correlated these spatial features with PFS and identified TiME
128 architectures that may be important for therapeutic decision making. Overall, we found

129 increased neoplastic tumor-immune cell spatial compartmentalization in primary tumors
130 to be associated with longer PFS. These tumors also contained alpha smooth muscle
131 actin (αSMA^+) cells with more organized structure located near T and B cells, as well as
132 near cells involved in antigen presentation. Our results are concordant with those from
133 other studies, indicating that the features identified herein are likely shared and
134 prognostic across cancer types.
135

136 # RESULTS

137 One to three regions of 2500^2 μm^2 from each of the nine patients primary and matched
138 recurrent tumor resections (n=18) were analyzed, for a total of 47 regions (**Table 1**,
139 **Figure 1a**). For this study, we utilized a gating strategy with thirteen lineage or
140 functional protein biomarkers to classify cells as neoplastic tumor cells, stromal cells
141 (mesenchymal), or one of seven different leukocyte subtypes spanning lymphoid and
142 myeloid lineages (**Table 2, Supplemental Figure 1a**). We investigated tumor
143 heterogeneity both within and across patient samples, quantified the cellular spatial
144 relationships within the TiME using a mixing score and performed a neighborhood
145 clustering method to describe the association between TiME spatial architecture, clinical
146 features, and PFS.
147

148 **Single-cell proteomic analyses reveal varying degrees of tumor heterogeneity**
149 To quantify how cellular composition varied across tumor regions, we assessed tumor
150 heterogeneity at multiple levels, including intra-tumoral, intra-patient, and inter-patient
151 cellular heterogeneity by calculating Kullback-Leibler (KL) divergences for each region,

152 performing hierarchical clustering, and conducting a principal component analysis
153 (PCA). The density of each cell type per region was measured for all eighteen tumor
154 specimens by taking the count of each cell type divided by the measured tissue area in
155 mm^2 (**Figure 1b,c**). We then calculated the coefficient of variation per cell type for each
156 tumor, and averaged these values to quantitatively describe the cell types contributing
157 most to intra-tumoral heterogeneity within the cohort. The coefficient of variation is
158 defined as the standard deviation divided by the mean, and it provides a normalized
159 measure of variability for comparison across cell types with large differences in
160 densities. On average, B cells exhibited the greatest coefficient of variation across the
161 cohort relative to other cell types (**Table 3**). This is likely due to the fact that B cells were
162 frequently observed to be spatially clustered together, resulting in regions of either high
163 B cell density or low B cell density despite being collected from the same tumor
164 (**Supplemental Figure 1b**).
165
166 To further quantify and assess tumor heterogeneity both within and across patients, we
167 calculated the KL divergence of each tumor region from five average cell type
168 distributions. KL divergence is a relative measure of how similar two distributions are,
169 with larger values reflecting less similarity between the distributions and smaller values
170 reflecting more similarity between the distributions. This measure has been used
171 previously to quantify tumor heterogeneity[6]. By calculating and comparing the
172 divergences of each tumor region from multiple average cell type distributions, we were
173 able to assess heterogeneity within and across tumors and patients. Overall, we
174 observed that heterogeneity was lower across regions from the same tumor and tumors

175 from the same patient (primary or recurrent), while higher across tumors from different
176 patients. This is evidenced by smaller intra-tumoral and intra-patient KL divergence
177 values for the majority of tumor regions (**Figure 1d**).
178
179 The cellular distributions used to calculate the five KL divergence values per tumor
180 region were (1) the average cellular distribution across all regions sampled from the
181 same tumor [“Intra-Tumor (P or R only)”]; (2) the average cellular distribution across the
182 patient’s primary and recurrent tumors [“Intra-Patient (P and R)”]; (3) the average
183 cellular distribution across all tumors in the cohort collected from the same timepoint
184 [“Inter-Patient (P or R only)”]; (4) the average cellular distribution across all tumors in
185 the cohort resected from the same anatomic site [“Inter-Patient (Same Anatomic Site)”],
186 and; (5) the average cellular distribution across all tumors collected from all patients in
187 the cohort, regardless of primary or recurrent status or anatomic site [“Inter-Patient
188 (all)”]. By comparing the relative KL divergence values to each other, we found tumor
189 regions to be more similar to regions sampled from the same tumor and patient than
190 regions collected from tumors of other patients. Notably, we found no significant
191 difference between “Inter-Patient (Same Anatomic Site)” and “Inter-Patient (all),”
192 indicating that tumor regions diverged by the same degree from regions sampled at the
193 same anatomic site as they did from regions sampled at all three anatomic sites (oral
194 cavity, oropharynx, larynx) of the head and neck region. Finally, given the large
195 proportion of neoplastic tumor cells comprising the TiME for many of the tumor regions,
196 we assessed KL divergence using only the distribution of immune cells present and
197 found similar results (**Supplemental Figure 1c**). This indicates that immune cell

198 composition is more similar within regions from the same patient than across regions
199 collected from different patients.
200
201 To further investigate intra-patient heterogeneity, we performed unsupervised
202 hierarchical clustering on the 47 tumor regions based on their normalized density
203 composition (**Figure 1e**). We found that two patients (3, green; 7, pink) contained all
204 tumor regions clustering together, independent of primary or recurrent state. These
205 patients also had the smallest intra-patient KL divergence values (**Figure 1d**), indicating
206 that the cell densities of these patients' primary and recurrent tumors were similar to
207 each other. Three patients (2, orange; 4, red; 9, yellow) contained nearly all regions
208 clustered together. The remaining four patients' tumors exhibited greater degrees of
209 intra-patient heterogeneity, as demonstrated by the distance between primary and
210 recurrent tumor regions on the clustered heatmap (**Figure 1e**). Overall, we found that
211 regions evaluated from the same patient tended to cluster together more than regions
212 evaluated from different patients (**Figure 1e**), indicating increased heterogeneity
213 between patients as compared to between samples from the same patient. We also
214 examined whether tumor regions clustered by the anatomic resection site and found
215 that the clusters formed did not group by site. These results, in addition to those of our
216 KL divergence analyses, indicate that anatomic site was likely not the main contributor
217 of cellular heterogeneity in this cohort. PCA results also supported these observations
218 (**Figure 1f,g**).
219
220 **TiME cellular composition altered by therapy**

221 Multiple studies have reported differences in TiME cellular makeup[25,26] and tumor clonal
222 diversity[27] between primary and recurrent tumors. To assess whether any immune
223 contexture changes occurred following post-operative therapy in our cohort, we
224 analyzed the cellular composition of primary tumors as compared to their recurrent
225 tumors. All patients received a combination therapy of cisplatin and/or cetuximab
226 accompanied by radiation following surgical resections of their primary tumors. We used
227 the average density of each cell type present across regions for a given tumor and
228 compared primary tumor composition to their matched recurrent tumor composition.
229 While we did not observe any significant differences in cell density between primary and
230 recurrent tumors ($p>0.112$), we did find that all patients experienced a decrease in the
231 density of B cells from their primary to recurrent tumors (**Figure 2a,b**). This result is
232 supported by a recent study that found that a large cohort of HNSCC patients
233 experienced a decline in B cells from primary to recurrent tumors, and this reduction
234 was dependent upon patients receiving adjuvant chemoradiotherapy[28]. We found no
235 common differences across all patients for any other cell type, although eight of the nine
236 patients saw a decrease in the density of neoplastic tumor cells from their primary to
237 recurrent tumors (**Figure 2b**).
238
239 We then assessed whether patients exhibited similar compositional differences in
240 primary and recurrent TiMEs by performing unsupervised hierarchical clustering on the
241 normalized average difference in cellular composition for each cell type. This resulted in
242 two groups of patients (**Figure 2c**). Interestingly, the two patients that received
243 cetuximab (2, orange; 5, purple), rather than cisplatin, clustered together within one of

244 these groups and were the only two patients to experience a decrease in the density of
245 every cell type following therapy. Across the cohort these patients had the greatest
246 decrease in the density of macrophages, granulocytes, and other $CD45^+$ immune cells
247 present from their primary tumors to their recurrent tumors following therapy (**Figure**
248 **2b,c)**. Interestingly, the one patient that received both cisplatin and cetuximab (7, pink)
249 was present in the other cluster from the two patients that received only cetuximab. This
250 was the only patient to experience an increase in the density of neoplastic tumor cells
251 (**Figure 2b,c**). This patient also experienced the second largest increase in $CD8^+$ T cells
252 as well as the greatest decrease in $CD4^+$ regulatory T cells, potentially indicating a pro-
253 inflammatory response to—or despite—increased neoplastic tumor cell density.
254 Altogether, these results indicate that shared trends in TiME composition changes from
255 primary to recurrent tumors specific to therapy exist, and regardless of therapy, all
256 patients exhibited a significant decrease in B cells from primary to recurrent tumors.
257
258 Approximately half (n=4) of the patients in the cohort experienced an increase in $CD8^+$ T
259 cell density while the other half (n=5) experienced a decrease in $CD8^+$ T cell density
260 following therapy. This was the only cell type that increased in density for nearly half of
261 the cohort and decreased for the other half. To determine if there was a survival
262 advantage for patients that experienced this increase, we split our cohort into short-term
263 or long-term survivor groups using median PFS and observed that all patients who
264 experienced an increase in $CD8^+$ T cell density from their primary to recurrent tumors
265 were long-term survivors (**Figure 2d**). Interestingly, the density of $CD8^+$ T cells in the
266 primary tumor alone did not associate with PFS (p=0.829). Prior research has revealed

267 that increased $CD8^+$ T cell abundance in the primary tumor is associated with better
268 outcomes in HNSCC[29-33]. However, these studies largely included HPV-positive
269 HNSCCs, which is more often associated with greater densities of $CD8^+$ T cells and
270 improved survival[22-24], thus unsurprising that our results differ. However, our results are
271 concordant with a recent study in HNSCC that reported longer survival was associated
272 with patients who had experienced an increase in $CD8^+$ tumor-infiltrating lymphocytes
273 from their primary to recurrent tumor[34]. Another study in HNSCC found a similar trend
274 between increased $CD8^+$ T cell infiltration, longer survival, presence of specific
275 neoantigens, and increased cytolytic activity in recurrent tumors[35]. Notably, the four
276 patients in our cohort that experienced the greatest decrease in $CD8^+$ T cell density in
277 recurrence had TNM stage 4 primary tumors, while patients that experienced an
278 increase in $CD8^+$ T cell density in recurrence included TNM stages 1, 2, 3, and 4.
279
280 **Quantifying the spatial organization of neoplastic and immune cells**
281 Prior studies reported the abundance of various cell types, including $CD8^+$ T cells[33],
282 $CD4^+$ regulatory T cells[36], and macrophages[37] to be associated with survival in HNSCC.
283 We analyzed the average density of each cell type across primary tumors for their
284 correlations with PFS, but found no significant association with PFS for any single cell
285 type ($p>0.159$). Given the prognostic potential of TiME cellular spatial organization as
286 has been reported in other cancer types[5-13], we quantified the spatial organization of
287 cells within tumor regions and examined the association of the spatial features with
288 clinical outcome.
289

290 We first deployed a mixing score, used previously to analyze immune cell spatial
291 compartmentalization in triple negative breast cancers[4]. The mixing score measures the
292 enrichment of neoplastic tumor-immune cell proximity relative to immune-immune cell
293 proximity within a set distance. We quantified the number of immune and neoplastic
294 tumor cells within 15 μm of each other, divided by the number of immune cells within 15
295 μm from another immune cell. Each region was labeled as mixed or compartmentalized
296 using the median mixing score value for all primary tumors as the threshold (**Figure**
297 **3a,b**; see Methods). This threshold classified tumor regions as mixed if at least one
298 neoplastic tumor cell was within 15 μm from an immune cell for approximately every ten
299 immune cells within 15 μm from another immune cell. Tumor regions were considered
300 compartmentalized when this ratio was smaller. Regions with fewer than 250 $CD45^+$
301 immune cells per 800^2 μm^2 present were labeled as cold, utilizing the same immune cell
302 density threshold from the original study[4]. Of the 47 total tumor regions, 25 were mixed,
303 20 were compartmentalized, and two were cold.
304
305 After calculating the mixing score for each region, we examined the spatial
306 heterogeneity of our cohort. Our tumor compositional heterogeneity analyses revealed
307 that intra-tumoral and intra-patient heterogeneity was less than inter-patient
308 heterogeneity. To determine whether this observation held for spatial organization
309 heterogeneity, we compared each region's mixing score to five groups of average
310 mixing scores, which were computed from the same five groups as the analysis in
311 Figure 1d: Intra-Tumor (P or R only), Intra-Patient (P and R), Inter-Patient (P or R only),
312 Inter-Patient (Same Anatomic Site), and Inter-Patient (all). Contrary to our analysis in

313 Figure 1d, the mixing score is only one feature, not a distribution of features, thus we
314 used the difference in mixing scores, rather than the KL divergence. In addition, we
315 calculated the absolute values of these differences as a way to normalize the data in
316 order to capture the degree of difference in spatial organization, allowing us to
317 subsequently test for differences across the five levels of heterogeneity. We found there
318 to be less intra-tumoral heterogeneity than inter-patient heterogeneity (**Supplemental**
319 **Figure 2a**). This result indicates that, in terms of neoplastic tumor-immune cell mixing,
320 tumor regions resemble regions sampled from the same tumor more than regions
321 sampled from tumors of other patients.
322
323 We then considered whether tumor regions sampled from the same anatomic site
324 differed in their spatial organization and found that of the three anatomic sites, tumor
325 regions from the oral cavity contained significantly different average mixing scores than
326 tumor regions from the larynx (p=0.016, **Figure 3c**). No significant differences were
327 found in average mixing scores between the oral cavity and the oropharynx or the
328 larynx and the oropharynx. Regions from larynx tumors did exhibit a greater range of
329 mixing scores than oral cavity or oropharynx (**Figure 3c**) indicating that larynx tumors
330 exhibit greater spatial heterogeneity in terms of neoplastic tumor-immune cell proximity.
331 We found no significant difference in the mixing scores of primary versus recurrent
332 tumors (Wilcoxon signed rank test, p=0.441).
333
334 **Spatial compartmentalization associated with longer progression free survival**

335 To investigate how spatial mixing correlated with patient outcome, we averaged the
336 mixing scores across regions and assigned a final mixing score and spatial label for
337 each tumor. Patients with more compartmentalization between neoplastic cells and
338 immune cells in their primary tumors exhibited significantly longer PFS than those with
339 greater mixing between these cell types (p=0.032, **Figure 3d**). We then examined how
340 the average mixing score of the tumors related to the TNM stage and anatomic site of
341 each primary tumor. Four of the five mixed primary tumors were TNM stage 4, and one
342 was TNM stage 1. The four compartmentalized primary tumors were TNM stages 1, 2,
343 3, and 4. All anatomic sites were present in both mixed and compartmentalized spatial
344 architecture groups (mixed: 2 oral cavity, 1 oropharynx, 2 larynx; compartmentalized: 2
345 oral cavity, 1 oropharynx, 1 larynx), indicating no single anatomic site had
346 predominantly mixed or compartmentalized spatial architecture.
347
348 **Spatial architecture associated with cellular composition**
349 We next explored how cellular composition related to spatial organization, in an effort to
350 explain the association found between mixing score and PFS. By coloring the initial
351 PCA on TiME composition by mixing score, we found that tumor regions from the same
352 mixing group clustered together (**Figure 3e**). Due to this association between cellular
353 composition and spatial organization, we wondered whether certain cell types would be
354 more frequent in mixed or compartmentalized tumors. Given how the mixing score is
355 calculated, we hypothesized that compartmentalized tumor regions would have greater
356 densities of immune cells than mixed regions, while mixed tumor regions would have
357 greater densities of neoplastic tumor cells than compartmentalized regions, and found

358 this to be the case (**Figure 3f**). Namely, compartmentalized tumor regions had greater
359 densities of $CD4^+$ T helper cells (p=0.016), B cells (p=0.048), antigen presenting cells
360 (APCs) (p=0.037), and other $CD45^+$ immune cells (p=0.048) than mixed tumor regions.
361 Given the role of $CD4^+$ T helper cells, B cells, and other $MHCII^+$ immune cells in antigen
362 presentation, these results could indicate enhanced antigen presentation in
363 compartmentalized tumor regions as compared to mixed regions. Conversely, mixed
364 tumor regions contained greater densities of neoplastic tumor cells than
365 compartmentalized regions (p<0.001).
366
367 We further examined associations between functional phenotypes of leukocytes and
368 mixing scores for each tumor region. Mixed regions contained a greater proportion of
369 lymphocytes, including $CD8^+$ T cells (p=0.023), $CD4^+$ T helper cells (p=0.017), and B
370 cells (p=0.016), expressing the immunoregulatory protein programmed death ligand
371 (PD)-1 than compartmentalized regions (**Figure 3g**). PD-1 is recognized as an indicator
372 of T cell antigen experience, whereas its expression on B cells has been reported to
373 suppress T cell effector function[38,39], indicating a suppressive and potentially
374 dysfunctional immune environment in mixed tumors. On the contrary,
375 compartmentalized regions contained a greater proportion of APCs expressing the
376 proliferation marker Ki-67 than mixed regions (p=0.032, **Figure 3h**), supporting the
377 notion that antigen presentation is a key feature of compartmentalized regions. We
378 performed a bootstrapping analysis to confirm the robustness of these results and
379 demonstrate that no one tumor was biasing the functional marker results
380 (**Supplemental Figure 2b,c,d,e**).

381

382 In addition to identifying differences between spatial architectures and their respective
383 immune and neoplastic tumor cell densities and functional marker expressions, we
384 found that tumor regions with more compartmentalization between neoplastic cells and
385 immune cells also contained greater densities of αSMA$^+$ mesenchymal cells, as
386 compared to those with higher mixing (p=0.002, **Figure 3f**). This result was intriguing
387 because these cells were not included when computing the mixing score, yet there is a
388 clear association between αSMA$^+$ cell density and the tumor's spatial organization
389 (**Figure 3i**).

390

391 **αSMA$^+$ mesenchymal spatial cellular neighborhoods reveal spatial landscapes**
392 **associated with progression free survival advantage**

393 Given the relationship between mixing score and αSMA$^+$ mesenchymal cell density, we
394 deployed a cellular neighborhood clustering analysis to identify which cell types were
395 spatially proximal to αSMA$^+$ cells across tumors in order to gain a better understanding
396 of whether these cells were contributing to the neoplastic tumor-immune spatial
397 compartmentalization observed. This analysis first involved calculating neighborhoods,
398 which were defined as physical groupings of cells within a set distance threshold from a
399 seed cell (**Figure 4a**). Each cell within the distance threshold was deemed a neighbor of
400 the seed cell, contributing to that seed cell's neighborhood's composition. After
401 identifying neighborhoods for each seed cell present across all tumor regions,
402 neighborhoods were grouped with K-means clustering, using the fraction of each cell

403 type present in the neighborhoods as the clustering features. This revealed clusters of
404 αSMA$^+$ cell neighborhoods with similar cellular makeups across all tumor regions.
405
406 We applied a neighborhood clustering analysis with αSMA$^+$ cells as the seed cells with
407 a distance threshold of 30 μm, as this produced neighborhoods with an average of
408 approximately ten neighbor cells. A recent study involving cellular neighborhood
409 analyses employed a method that selected the ten nearest spatial neighbors of the seed
410 cell, regardless of the distance between the seed cell and its neighbors[7]. By setting a
411 distance threshold of 30 μm, our method required the cells be close, if not directly
412 touching, while still capturing enough neighbors to cluster on. Any αSMA$^+$ cell that did
413 not have any neighbors was removed from downstream clustering analyses. Clustering
414 results yielded seven groups, each different in their average composition of αSMA$^+$
415 neighborhoods (**Figure 4b**). Clusters 1 and 2 contained mostly other αSMA$^+$ cells
416 comprising the neighborhoods; in fact, cluster 1 was almost exclusively made up of
417 αSMA$^+$ cells. Cluster 3 contained the greatest proportion of neoplastic tumor cell
418 neighbors. Clusters 4, 5, 6, and 7 were all comprised of roughly 75% immune cells as
419 neighbors, although they differed in the types of immune cells present. Cluster 4 was
420 defined by a majority of other CD45$^+$ immune cells not explicitly defined within our
421 gating strategy. To elucidate marker expression within these other CD45$^+$ cells, we
422 performed a post-hoc t-distributed stochastic neighbor embedding (t-SNE) analysis on
423 cells classified as 'other immune,' and found them to contain a large population of
424 CD163$^+$ cells and a smaller population of mast cells (tryptase$^+$) (**Supplemental Figure**
425 **3a**). Cluster 5 contained primarily CD8$^+$ T cells as the dominant immune population.

426 Cluster 6 consisted of CD4$^+$ T helper cells, B cells, and the greatest proportion of APCs
427 of any cluster. Finally, cluster 7 was defined by its large proportion of granulocytes.
428
429 We confirmed that no single tumor region, entire tumor, or patient dominated any of the
430 αSMA$^+$ neighborhood clusters by examining the percent contribution of each of the
431 seven clusters per 47 tumor regions, eighteen tumors, and nine patients. While clusters
432 were present in varying degrees across tumor regions, our results indicated that no
433 region (**Supplemental Figure 3b**), tumor (**Supplemental Figure 3c**), or patient
434 (**Supplemental Figure 3d**) was solely responsible for giving rise to any of the clusters.
435 We also confirmed that all seven clusters were present in tumors collected from each of
436 the three anatomic sites (**Supplemental Figure 3e**), as well as each of the four TNM
437 stages (**Supplemental Figure 3f**).
438
439 To identify groups of patients with primary tumors of similar αSMA$^+$ cellular
440 neighborhoods, we performed unsupervised hierarchical clustering on the normalized
441 average αSMA$^+$ cellular neighborhood composition across the nine primary tumors. This
442 resulted in two groups of patients, differing in proportional compositions of αSMA$^+$
443 cellular neighborhoods (**Figure 4c**). On average, both groups had roughly 20% of their
444 αSMA$^+$ cells assigned to cluster 2 and roughly 10% of their αSMA$^+$ cells assigned to
445 cluster 5 (**Figure 4d**). However, the two groups differed in that group 1 (blue) included
446 patients with αSMA$^+$ cells predominantly assigned to clusters 1 and 6, meaning their
447 αSMA$^+$ cells were primarily surrounded by CD4$^+$ T helper cells, B cells, and other
448 αSMA$^+$ cells. On the contrary, group 2 (orange) included patients with more of their

449 αSMA$^+$ cells assigned to clusters 3, 4, and 7, meaning their αSMA$^+$ cells were mostly
450 surrounded by neoplastic tumor cells, other immune cells, and granulocytes. Consistent
451 with our results, visualization of tissue regions illustrates primary tumors in group 1
452 containing more αSMA$^+$ stromal cells overall, frequently neighboring CD4$^+$ T helper cells
453 and B cells, with greater MHCII positivity (**Figure 4e**). Primary tumors in group 2
454 contained less structured αSMA$^+$ stromal cells, fewer neighboring immune cells, and
455 less MHCII positivity, differences that were strikingly apparent in the mIHC stained
456 tissue images (**Figure 4e**). Despite both groups containing nearly equal proportions of
457 CD8$^+$ T cells neighboring αSMA$^+$ cells, group 1 contained higher densities of CD4$^+$ T
458 cells and increased MHCII positivity as compared to group 2 (**Figure 4e**).
459
460 To determine if the composition of αSMA$^+$ cellular neighborhood groups was correlated
461 with clinical outcome, we performed a survival analysis on the two groups of patients.
462 We found that patients in group 1 had significantly longer PFS than patients in group 2
463 ($p=0.047$, **Figure 4f**). Patients in group 1 had primary tumors annotated as TNM stages
464 1, 2, 3, and 4, while patients in group 2 had four primary tumors annotated as TNM
465 stage 4 and one annotated as TNM stage 1. Tumors from all three anatomic sites were
466 represented in both groups. An analysis of the proportions of αSMA$^+$ neighborhood
467 clusters present in each of the nine primary tumors revealed the varying degrees to
468 which each of the seven clusters were present in each of the tumors (**Figure 4g**).
469 Notably, we found there to be a positive correlation between the presence of clusters 1
470 and 6 ($r = +0.69$) as well as clusters 4 and 7 ($r = +0.66$). We found negative correlations
471 between the presence of clusters 1 and 4 ($r = -0.88$), clusters 3 and 6 ($r = -0.69$), and

472 clusters 6 and 7 (r = -0.65). Finally, we found the two groups resulting from hierarchical
473 clustering to be associated with mixing status. Specifically, group 1 consisted of 75%
474 compartmentalized tumors, and group 2 consisted of 80% mixed tumors. Overall, these
475 results describe interesting spatial relationships between immune cells, mesenchymal
476 stroma, and neoplastic tumor cells, indicating increased antigen presentation and
477 immune activity associated with compartmentalization and progression free survival.
478

479 **DISCUSSION**

480 The significant role that TiME cellular composition plays in tumor progression and
481 response to therapy has been accepted for over a decade[40]. However, recent findings
482 powered by single-cell proteomics imaging technologies have found that the spatial
483 organization of the cells present in the TiME also plays a critical role[4-13]. TiME spatial
484 quantifications are just beginning to provide novel insights into tumor biology, and thus it
485 is still unclear exactly which spatial features are important in dictating response to
486 therapy or clinical outcome, as well as whether these features are shared across cancer
487 types, and how they could be leveraged for therapeutic decisions and patient
488 stratification. Here, we leveraged single-cell spatial proteomics data generated by our
489 mIHC immunoassay-based imaging platform to quantitatively assess the TiME of nine
490 matched primary and recurrent HPV(-) HNSCCs in order to demonstrate the use of
491 spatial features in disease prognosis. Our results provide novel insights into the
492 heterogeneity and spatial landscape of HPV(-) HNSCCs, and highlight possible TiME
493 spatial landscapes that may impact clinical outcome across cancer types.
494

495 We found concordance between the results from our heterogeneity and composition
496 analyses and those from several other studies. Our results are similar to a study that
497 clustered HNSCC biopsies based on their neoplastic and immune gene signatures as
498 determined by RNA-sequencing, and reported that samples from the same patient were
499 more similar to each other than samples from different patients[41]. This trend has also
500 been observed across cancer types, including melanoma[42], hepatocellular carcinoma[43],
501 pancreatic ductal adenocarcinoma[44], and breast cancer[45]. Moreover, we found that
502 patients who experienced an increase in $CD8^+$ T cell density from their primary to
503 recurrent tumors were associated with improved PFS, which has previously been
504 reported in head and neck cancer[34,35]. Conversely, patients experiencing the greatest
505 decrease in $CD8^+$ T cell density in recurrence had TNM stage 4 primary tumors. This
506 could indicate that later staged primary tumors are better equipped to evade immune
507 attack in recurrence, and a therapy to elicit an anti-tumor immune response may be
508 beneficial.
509
510 Despite the fact that HPV(-) HNSCCs often contain limited immune infiltrates[22], our
511 analyses revealed significant differences in the immune cell spatial organization within
512 these tumors that were associated with progression free survival, highlighting the
513 importance of considering the spatial context of the TiME. Most strikingly, patients
514 whose primary tumors contained more compartmentalization between their neoplastic
515 tumor cell and immune cell populations demonstrated longer PFS. This correlation was
516 also identified in a similar analysis of triple negative breast cancer patients[4], indicating
517 that a compartmentalized spatial architecture may play a favorable role in survival

518 across cancer types. Our analyses of TiME composition and functional marker
519 expression indicate there is likely more antigen presentation and less immunoregulation
520 in regions of compartmentalization rather than in regions of mixing. This favorable
521 immune landscape in compartmentalized tumors may contribute to improved survival.
522 On the contrary, four of the five of the mixed primary tumors were classified as TNM
523 stage 4, which may contribute to shortened survival for these patients. However, given
524 that compartmentalized tumors were not all classified as an early TNM stage and
525 instead ranged from TNM stage 1 to 4, it is difficult to determine the exact association
526 between neoplastic tumor and immune cell mixing versus TNM stage, and further
527 investigation is warranted to understand these correlations and impact on prognosis.
528
529 Prior studies have identified a mesenchymal HNSCC subtype[46,47]; our αSMA$^+$
530 mesenchymal cellular neighborhood analyses highlight the importance of considering
531 how these cells are organized within the TiME, beyond simply considering their
532 presence in the tumor. This could reveal more precise mesenchymal subtypes for
533 improved stratification for patient care. αSMA is a common marker for cancer-
534 associated fibroblasts (CAFs)[20,48], whose presence in tumors, including HNSCC, tends
535 to be associated with tumor progression, metastasis, and resistance to therapy[49-54].
536 However, despite compartmentalized tumors having increased αSMA$^+$ cell density,
537 patients with compartmentalized primary tumors demonstrated longer PFS, which
538 indicates that the spatial organization of αSMA$^+$ cells may be related to their function.
539

540 We found αSMA$^+$ cells neighboring immune cells in both mixed and compartmentalized
541 primary tumors, but the types of immune cells near αSMA$^+$ cells differed. This is
542 interesting, as emerging research has found that CAFs, which are often defined by their
543 expression of αSMA, can modulate immune cell function within the TiME. With our
544 mIHC platform we were able to identify the differences in the types of immune cells
545 neighboring αSMA$^+$ cells and relate these differences to survival, supporting recent
546 research on the impact of CAFs on various immune cell populations. A recent study in
547 melanoma found CAFs to be instrumental in aiding tertiary lymphoid structure (TLS)
548 development[55]; TLS are defined by their large concentration of B cells surrounded by T
549 cells, and their presence in tumors is associated with improved patient outcome[3,56,57]. In
550 compartmentalized tumors, we noticed the αSMA$^+$ cells to be more structured and
551 located neighboring dense pockets of T cells and B cells, perhaps indicating the
552 formation of TLS. Although this antibody panels did not include a biomarker for high
553 endothelial venules to confirm presence of TLS, our results support the notion that CAF-
554 lymphocyte interactions can be clinically beneficial.
555
556 Conversely, patients with predominantly mixed primary tumors and shorter PFS
557 contained αSMA$^+$ cells primarily located near granulocytes and other CD45$^+$ immune
558 cells, many of which were likely CD163$^+$ myelomonocytic cells or mast cells. CD163 is a
559 marker for scavenger receptor activity and is commonly used to demark pro-tumor type
560 tumor-associated macrophages and monocytes. Supporting these findings, a study in
561 oral squamous cell carcinoma found the presence of CAFs to be associated with
562 increased presence of CD163$^+$ macrophages and worse survival[58]. Another study

563 reported CAFs to be correlated with an increase in monocyte expression of CD163,
564 which in turn suppressed T cell proliferation and increased neoplastic cell proliferation in
565 breast cancer[59]. Mast cells mediate innate and acquired immune response as a part of
566 the myeloid lineage. They have been reported to facilitate neo-vascularization and
567 tumor dissemination in HNSCC, and found to be correlated with increased angiogenesis
568 in advanced HNSCC[60]. However, interactions between mast cells and CAFs is largely
569 unknown; our results indicate this interaction may be associated with increased
570 neoplastic density and worse PFS. Of note, a recent study in melanoma and pancreatic
571 adenocarcinoma found neutrophils, a subclass of granulocytes, to exert pro-tumor
572 effects when in the presence of CAFs[61], and another study found the combined
573 presence of neutrophils and CAFs to be associated with shortened survival in gastric
574 adenocarcinoma[62].
575
576 Finally, patients with predominantly mixed primary tumors and shorter PFS were found
577 to contain fewer overall stromal cells and greater proportions of those αSMA$^+$ cells
578 neighboring neoplastic tumor cells. It has been reported that neoplastic tumor cells in
579 direct contact with CAFs move along tracks laid by the CAFs in the extracellular matrix,
580 promoting tumor growth[63,64]. It is possible that αSMA$^+$ cells in mixed tumors may provide
581 avenues for neoplastic tumor cells to transit, thus leading to more advanced tumor
582 progression. Overall, spatial analyses herein deepened our understanding of neoplastic
583 tumor and immune cell organization relative to each other, and how this organization is
584 related to αSMA$^+$ cells working in tandem with many cells, beyond single cell-cell
585 interactions, to impact TiME organization, and ultimately, clinical outcome. The

586 conclusions from our spatial analyses and their relationship to clinical variables are
587 summarized in **Figure 5**.
588
589 The concordance found among results herein and those of the aforementioned studies
590 provides orthogonal support for our conclusions and indicates that single-cell
591 heterogeneity and spatial organization of tumors may share similarities across different
592 types of cancer and across different molecular assays. Our spatial analyses
593 demonstrate the use of various algorithms to quantify the spatial landscape of tumors
594 using single-cell imaging data. Further, our computational methods provide a framework
595 for future single-cell imaging analyses, as they are applicable to any multiplex imaging
596 assay, including mIHC, co-detection by indexing technology (CODEX)[7], cyclic
597 immunofluorescence[18,65,66], and imaging mass cytometry[6]. Our results highlight several
598 spatial architectures that may help guide precision medicine approaches for HPV(-)
599 HNSCC patients, including architectures that may help stratify patients who may have
600 shorter PFS, and thus warrant more aggressive therapy or clinical follow-ups. While our
601 results provide evidence that the spatial organization of HPV(-) HNSCC tumors
602 correlates with clinical outcome, future studies with larger cohorts will be needed to
603 evaluate the strength and validity of our observations. Studies with greater
604 representation of anatomic site and stage are also needed to assess the prognostic
605 value of the spatial features identified in this HNSCC cohort. Despite these limitations,
606 this study demonstrates practical analysis strategies that elucidate spatial architecture
607 features for potential use in precision medicine.
608

609 # METHODS

610 **Multiplex immunohistochemistry data generation**

611 mIHC is an immunohistochemical-based imaging platform that evaluates sequentially
612 stained immune lineage epitope-specific antibodies for immunodetection on FFPE
613 tissue sections[16,17]. Images were stained and processed as described in our previous
614 report[17]. A table of antibodies, species, vendor, and concentration used in staining are
615 previously reported in Table 1 of Banik et al[17]. Briefly, sequentially stained images were
616 co-registered in MATLAB. AEC signal from each antibody stain was extracted and
617 normalized, and the mean intensity of each single cell for each marker was quantified in
618 Cell Profiler. Watershed based nuclei segmentation on hematoxylin staining was used
619 to identify single cells in FIJI. Using a hierarchical gating strategy, single cells were
620 phenotyped using image gating cytometry in FCS Express 7 Image Cytometry RUO
621 (**Supplemental Figure 1a**). A threshold was set on the scatterplot of mean intensity for
622 each marker within the gating strategy, validated by visual live rendering of masked cell
623 objects within the selected gate on extracted marker signals. Cartesian coordinates of
624 each phenotyped cell were maintained relative to the tissue region.

625

626 We applied the mIHC pipeline to analyze matched primary and recurrent FFPE tissue
627 specimens from nine HPV(-) HNSCC patients. Each patient underwent surgical
628 resection of their primary tumor prior to beginning a regimen of chemotherapy and
629 radiation therapy. Upon recurrence, the patient underwent another surgical resection of
630 their recurrent tumor. Tissue specimens for each patient were obtained from the Oregon
631 Health & Science University Knight Biolibrary and were deidentified and coded with a

632 unique identifier prior to analysis. Patient demographic and clinical data including HPV
633 status, tobacco and alcohol use, treatment regimens, and survival outcomes were
634 collected. All HNSCC tumors were staged according to the 8th edition AJCC/UIC TNM
635 classification and cohort characteristics are shown in **Table 1** as reported in Banik et
636 al[17]. All studies involving human tissue were approved by institutional IRB (protocol
637 #809 and #3609), and written informed consent was obtained.
638
639 **Tumor heterogeneity analyses**
640 The Kullback-Leibler divergence was calculated using the entropy function from the
641 Scipy Python package[67]. The distribution of each individual tumor region's cellular
642 composition was compared to the average of five different cellular composition
643 distributions: the average distribution for the region's tumor, the average distribution for
644 the patient's primary and recurrent tumors, the average distribution across all tumors of
645 the same timepoint in the cohort (primary or recurrent), the average distribution across
646 all tumors resected from the same anatomic site in the cohort, and the average
647 distribution across all tumors from all patients in the cohort (primary and recurrent
648 combined). Log base 2 was used for the calculation. Unsupervised hierarchical
649 clustering of each tumor region was performed using the log10+1 normalized density of
650 each cell type present as the features. Euclidean distance was used to determine
651 distances between observations, and the Ward method was used for the linkage.
652
653 **TiME compositional change clustering analysis**

654 Unsupervised hierarchical clustering of each patient was performed using the
655 normalized change in density of each cell type as the features. Euclidean distance was
656 used to determine distances between observations, and the Ward method was used for
657 the linkage. Normalization in the change in density was computing by first calculating
658 the absolute value of the raw change in density for each cell type. These values were
659 then normalized to a range of [0,1]. Finally, the values that were originally negative
660 (decreasing change), were flipped to be negative values again, such that all values
661 ranged from [-1,1] with zero representing no change.
662
663 **Mixing score analysis**
664 Keren et al. developed a mixing score to quantify the ratio of neoplastic and immune cell
665 spatial interactions[4]. This score is defined as the number of interactions between
666 neoplastic tumor cells and immune cells divided by the number of interactions between
667 immune cells and another immune cell within a tumor region. We defined there to be an
668 interaction between two cells if their centers [the (x,y) coordinates provided by mIHC]
669 were within 15 μm from one another. We used the median mixing score value (0.107)
670 for all primary tumors as the threshold to distinguish between mixed and
671 compartmentalized spatial organization groups. Tumor regions with a mixing score of
672 greater than 0.107 were defined as mixed. Tumor regions with a mixing score of less
673 than 0.107 were defined as compartmentalized. We used a density threshold of less
674 than 250 immune cells per 800^2 μm^2 to define tumor regions as cold. We chose this
675 threshold to match that used by Keren et al.
676

677 **Functional marker bootstrapping analyses**

678 Bootstrapping analyses involved the following steps. First, one tumor region per
679 eighteen tumor samples was randomly selected. The regions were then split into two
680 groups based on their mixed or compartmentalized spatial architecture designation, and
681 the average proportion of the specified cell population expressing the specified
682 functional marker was calculated for each group. Finally, this process was repeated 100
683 times, yielding 100 values representing the proportion of the specified cell population
684 expressing the specified functional marker for mixed tumor regions and 100 values
685 representing the proportion of the specified cell population expressing the specified
686 functional marker for compartmentalized tumor regions. These values were then
687 compared between the mixed and compartmentalized groups for differences.

688

689 **Cellular neighborhood clustering analyses**

690 Cellular neighborhoods were defined by drawing a circle of a specified radius around all
691 seed cells of a given phenotype. Cells whose centers were inside the circle were
692 considered neighbors of that seed cell and contributed to that cell's neighborhood. All
693 neighborhoods across all tumor regions were then clustered using scikit-learn's
694 MiniBatchKMeans function[68] to perform K-means clustering according to their
695 normalized cellular composition. The elbow method was used to determine the number
696 of clusters to form. Each resulting cluster was comprised of neighborhoods with a
697 similar cellular makeup. Unsupervised hierarchical clustering of each primary tumor was
698 performed using the log10+1 normalized proportion (out of 100) of αSMA^+ cell
699 neighborhood clusters present in the tumor as the features. Euclidean distance was

700 used to determine distances between observations, and the Ward method was used for
701 the linkage.
702
703 **Statistics**
704 Independent t-tests were used to determine statistically significant differences for
705 independent samples whose differences followed a normal distribution. Mann-Whitney
706 U tests were used to determine statistically significant differences for independent
707 samples whose differences did not follow a normal distribution. Paired t-tests were used
708 to determine statistically significant differences for paired samples whose differences
709 followed a normal distribution. Wilcoxon signed rank tests were used to determine
710 statistically significant differences for paired samples whose differences did not follow a
711 normal distribution. One-way ANOVA tests were used to determine statistically
712 significant differences for multi-group comparisons. If the ANOVA result was significant,
713 a Tukey honestly significant difference post-hoc test was conducted to determine which
714 groups were significantly different from one another. A Benjamini-Hochberg correction
715 was used to account for multiple hypothesis testing in analyses that involved
716 systematically testing multiple variables. P-values less than 0.05 were considered
717 statistically significant. All statistical calculations were performed with the Scipy and
718 statsmodels packages using Python software[67,69].
719
720 **Survival analyses**

721 Kaplan-Meier curves were generated and a log-rank test was performed using the
722 lifelines package with Python software[70]. P-values less than 0.05 were considered
723 statistically significant.
724
725 **Data and software availability**
726 All of the data produced by our mIHC computational image processing pipeline,
727 including protein abundance, cell phenotype, and cell location information saved in the
728 form of a matrix, in addition to survival data, is available for download at Zenodo
729 (https://doi.org/10.5281/zenodo.5540356). All computational analyses in this study were
730 performed using Python software, version 3.6.5. The code created to produce the
731 results of this study is available at https://github.com/kblise/HNSCC_mIHC_paper.
732

733 ## ACKNOWLEDGEMENTS

734 The authors thank Dr. Courtney Betts, Justin Tibbitts, Teresa Beechwood, and Meghan
735 Lavoie for regulatory and technical assistance. The authors thank the OHSU Knight
736 Biostatistics Shared Resource for guidance with statistical calculations. The authors
737 also acknowledge and thank the patients who donated tissue samples for this study.

REFERENCES

1 Binnewies, M. *et al.* Understanding the tumor immune microenvironment (TIME) for effective therapy. *Nat Med* **24**, 541-550 doi:10.1038/s41591-018-0014-x (2018).

2 Junttila, M. R. & de Sauvage, F. J. Influence of tumour micro-environment heterogeneity on therapeutic response. *Nature* **501**, 346-354 doi:10.1038/nature12626 (2013).

3 Petitprez, F. *et al.* B cells are associated with survival and immunotherapy response in sarcoma. *Nature* **577**, 556-560 doi:10.1038/s41586-019-1906-8 (2020).

4 Keren, L. *et al.* A Structured Tumor-Immune Microenvironment in Triple Negative Breast Cancer Revealed by Multiplexed Ion Beam Imaging. *Cell* **174**, 1373-1387 e1319 doi:10.1016/j.cell.2018.08.039 (2018).

5 Ali, H. R. *et al.* Imaging mass cytometry and multiplatform genomics define the phenogenomic landscape of breast cancer. *Nature Cancer* **1**, 163-175 doi:10.1038/s43018-020-0026-6 (2020).

6 Jackson, H. W. *et al.* The single-cell pathology landscape of breast cancer. *Nature* **578**, 615-620 doi:10.1038/s41586-019-1876-x (2020).

7 Schurch, C. M. *et al.* Coordinated Cellular Neighborhoods Orchestrate Antitumoral Immunity at the Colorectal Cancer Invasive Front. *Cell* doi:10.1016/j.cell.2020.07.005 (2020).

8 Farkkila, A. *et al.* Immunogenomic profiling determines responses to combined PARP and PD-1 inhibition in ovarian cancer. *Nat Commun* **11**, 1459 doi:10.1038/s41467-020-15315-8 (2020).

9 Barua, S. *et al.* Spatial interaction of tumor cells and regulatory T cells correlates with survival in non-small cell lung cancer. *Lung Cancer* **117**, 73-79 doi:10.1016/j.lungcan.2018.01.022 (2018).

10 Gide, T. N. *et al.* Close proximity of immune and tumor cells underlies response to anti-PD-1 based therapies in metastatic melanoma patients. *Oncoimmunology* **9**, 1659093 doi:10.1080/2162402X.2019.1659093 (2020).

11 Giraldo, N. A. *et al.* Multidimensional, quantitative assessment of PD-1/PD-L1 expression in patients with Merkel cell carcinoma and association with response to pembrolizumab. *J Immunother Cancer* **6**, 99 doi:10.1186/s40425-018-0404-0 (2018).

12 Johnson, D. B. *et al.* Quantitative Spatial Profiling of PD-1/PD-L1 Interaction and HLA-DR/IDO-1 Predicts Improved Outcomes of Anti-PD-1 Therapies in Metastatic Melanoma. *Clin Cancer Res* **24**, 5250-5260 doi:10.1158/1078-0432.CCR-18-0309 (2018).

13 Enfield, K. S. S. *et al.* Hyperspectral cell sociology reveals spatial tumor-immune cell interactions associated with lung cancer recurrence. *J Immunother Cancer* **7**, 13 doi:10.1186/s40425-018-0488-6 (2019).

14 Galon, J. *et al.* Type, density, and location of immune cells within human colorectal tumors predict clinical outcome. *Science* **313**, 1960-1964 doi:10.1126/science.1129139 (2006).

15 Galon, J. *et al.* Cancer classification using the Immunoscore: a worldwide task force. *J. Transl. Med.* **10**, 205 doi:10.1186/1479-5876-10-205 (2012).
16 Tsujikawa, T. *et al.* Quantitative Multiplex Immunohistochemistry Reveals Myeloid-Inflamed Tumor-Immune Complexity Associated with Poor Prognosis. *Cell Rep* **19**, 203-217 doi:10.1016/j.celrep.2017.03.037 (2017).
17 Banik, G. *et al.* High-dimensional multiplexed immunohistochemical characterization of immune contexture in human cancers. *Methods Enzymol* **635**, 1-20 doi:10.1016/bs.mie.2019.05.039 (2020).
18 Eng, J. *et al.* Cyclic Multiplexed-Immunofluorescence (cmIF), a Highly Multiplexed Method for Single-Cell Analysis. *Methods Mol. Biol.* **2055**, 521-562 doi:10.1007/978-1-4939-9773-2_24 (2020).
19 Brucher, B. L. & Jamall, I. S. Cell-cell communication in the tumor microenvironment, carcinogenesis, and anticancer treatment. *Cell. Physiol. Biochem.* **34**, 213-243 doi:10.1159/000362978 (2014).
20 Alsahafi, E. *et al.* Clinical update on head and neck cancer: molecular biology and ongoing challenges. *Cell Death Dis.* **10**, 540 doi:10.1038/s41419-019-1769-9 (2019).
21 Cohen, E. E. W. *et al.* The Society for Immunotherapy of Cancer consensus statement on immunotherapy for the treatment of squamous cell carcinoma of the head and neck (HNSCC). *J Immunother Cancer* **7**, 184 doi:10.1186/s40425-019-0662-5 (2019).
22 Canning, M. *et al.* Heterogeneity of the Head and Neck Squamous Cell Carcinoma Immune Landscape and Its Impact on Immunotherapy. *Front Cell Dev Biol* **7**, 52 doi:10.3389/fcell.2019.00052 (2019).
23 Fakhry, C. *et al.* Improved survival of patients with human papillomavirus-positive head and neck squamous cell carcinoma in a prospective clinical trial. *J. Natl. Cancer Inst.* **100**, 261-269 doi:10.1093/jnci/djn011 (2008).
24 Ang, K. K. *et al.* Human papillomavirus and survival of patients with oropharyngeal cancer. *N. Engl. J. Med.* **363**, 24-35 doi:10.1056/NEJMoa0912217 (2010).
25 Predina, J. *et al.* Changes in the local tumor microenvironment in recurrent cancers may explain the failure of vaccines after surgery. *Proc. Natl. Acad. Sci. U. S. A.* **110**, E415-424 doi:10.1073/pnas.1211850110 (2013).
26 Zheng, B. *et al.* Changes in the tumor immune microenvironment in resected recurrent soft tissue sarcomas. *Ann Transl Med* **7**, 387 doi:10.21037/atm.2019.07.43 (2019).
27 Walens, A. *et al.* Adaptation and selection shape clonal evolution of tumors during residual disease and recurrence. *Nat Commun* **11**, 5017 doi:10.1038/s41467-020-18730-z (2020).
28 Watermann, C. *et al.* Recurrent HNSCC Harbor an Immunosuppressive Tumor Immune Microenvironment Suggesting Successful Tumor Immune Evasion. *Clin Cancer Res* **27**, 632-644 doi:10.1158/1078-0432.CCR-20-0197 (2021).
29 Hartman, D. J., Ahmad, F., Ferris, R. L., Rimm, D. L. & Pantanowitz, L. Utility of CD8 score by automated quantitative image analysis in head and neck squamous cell carcinoma. *Oral Oncol.* **86**, 278-287 doi:10.1016/j.oraloncology.2018.10.005 (2018).

30 Balermpas, P. *et al.* CD8+ tumour-infiltrating lymphocytes in relation to HPV status and clinical outcome in patients with head and neck cancer after postoperative chemoradiotherapy: A multicentre study of the German cancer consortium radiation oncology group (DKTK-ROG). *Int. J. Cancer* **138**, 171-181 doi:10.1002/ijc.29683 (2016).
31 Nasman, A. *et al.* Tumor infiltrating CD8+ and Foxp3+ lymphocytes correlate to clinical outcome and human papillomavirus (HPV) status in tonsillar cancer. *PLoS One* **7**, e38711 doi:10.1371/journal.pone.0038711 (2012).
32 Nordfors, C. *et al.* CD8+ and CD4+ tumour infiltrating lymphocytes in relation to human papillomavirus status and clinical outcome in tonsillar and base of tongue squamous cell carcinoma. *Eur. J. Cancer* **49**, 2522-2530 doi:10.1016/j.ejca.2013.03.019 (2013).
33 Balermpas, P. *et al.* Tumour-infiltrating lymphocytes predict response to definitive chemoradiotherapy in head and neck cancer. *Br. J. Cancer* **110**, 501-509 doi:10.1038/bjc.2013.640 (2014).
34 So, Y. K. *et al.* An increase of CD8(+) T cell infiltration following recurrence is a good prognosticator in HNSCC. *Sci. Rep.* **10**, 20059 doi:10.1038/s41598-020-77036-8 (2020).
35 Schutt, C. R. *et al.* Genomic and neoantigen evolution from primary tumor to first metastases in head and neck squamous cell carcinoma. *Oncotarget* **12**, 534-548 doi:10.18632/oncotarget.27907 (2021).
36 Russell, S. *et al.* Immune cell infiltration patterns and survival in head and neck squamous cell carcinoma. *Head Neck Oncol.* **5**, 24 (2013).
37 Wolf, G. T. *et al.* Tumor infiltrating lymphocytes (TIL) and prognosis in oral cavity squamous carcinoma: a preliminary study. *Oral Oncol.* **51**, 90-95 doi:10.1016/j.oraloncology.2014.09.006 (2015).
38 Wang, X. *et al.* PD-1-expressing B cells suppress CD4(+) and CD8(+) T cells via PD-1/PD-L1-dependent pathway. *Mol. Immunol.* **109**, 20-26 doi:10.1016/j.molimm.2019.02.009 (2019).
39 Thibult, M. L. *et al.* PD-1 is a novel regulator of human B-cell activation. *Int. Immunol.* **25**, 129-137 doi:10.1093/intimm/dxs098 (2013).
40 Fridman, W. H., Pages, F., Sautes-Fridman, C. & Galon, J. The immune contexture in human tumours: impact on clinical outcome. *Nat. Rev. Cancer* **12**, 298-306 doi:10.1038/nrc3245 (2012).
41 Wood, O. *et al.* Head and Neck Squamous Cell Carcinomas Are Characterized by a Stable Immune Signature Within the Primary Tumor Over Time and Space. *Clin Cancer Res* **23**, 7641-7649 doi:10.1158/1078-0432.CCR-17-0373 (2017).
42 Reuben, A. *et al.* Genomic and immune heterogeneity are associated with differential responses to therapy in melanoma. *NPJ Genom Med* **2** doi:10.1038/s41525-017-0013-8 (2017).
43 Zhang, Q. *et al.* Integrated multiomic analysis reveals comprehensive tumour heterogeneity and novel immunophenotypic classification in hepatocellular carcinomas. *Gut* **68**, 2019-2031 doi:10.1136/gutjnl-2019-318912 (2019).
44 Lin, W. *et al.* Single-cell transcriptome analysis of tumor and stromal compartments of pancreatic ductal adenocarcinoma primary tumors and

874 metastatic lesions. *Genome Med.* **12**, 80 doi:10.1186/s13073-020-00776-9
875 (2020).
876 45 Gyanchandani, R. *et al.* Intratumor Heterogeneity Affects Gene Expression
877 Profile Test Prognostic Risk Stratification in Early Breast Cancer. *Clin Cancer*
878 *Res* **22**, 5362-5369 doi:10.1158/1078-0432.CCR-15-2889 (2016).
879 46 Chung, C. H. *et al.* Molecular classification of head and neck squamous cell
880 carcinomas using patterns of gene expression. *Cancer Cell* **5**, 489-500
881 doi:10.1016/s1535-6108(04)00112-6 (2004).
882 47 Walter, V. *et al.* Molecular subtypes in head and neck cancer exhibit distinct
883 patterns of chromosomal gain and loss of canonical cancer genes. *PLoS One* **8**,
884 e56823 doi:10.1371/journal.pone.0056823 (2013).
885 48 Parajuli, H. *et al.* Integrin alpha11 is overexpressed by tumour stroma of head
886 and neck squamous cell carcinoma and correlates positively with alpha smooth
887 muscle actin expression. *J. Oral Pathol. Med.* **46**, 267-275 doi:10.1111/jop.12493
888 (2017).
889 49 Zhang, Q. *et al.* Integrated analysis of single-cell RNA-seq and bulk RNA-seq
890 reveals distinct cancer-associated fibroblasts in head and neck squamous cell
891 carcinoma. *Ann Transl Med* **9**, 1017 doi:10.21037/atm-21-2767 (2021).
892 50 Lim, K. P. *et al.* Fibroblast gene expression profile reflects the stage of tumour
893 progression in oral squamous cell carcinoma. *J. Pathol.* **223**, 459-469
894 doi:10.1002/path.2841 (2011).
895 51 Shiga, K. *et al.* Cancer-Associated Fibroblasts: Their Characteristics and Their
896 Roles in Tumor Growth. *Cancers (Basel)* **7**, 2443-2458
897 doi:10.3390/cancers7040902 (2015).
898 52 Tao, L., Huang, G., Song, H., Chen, Y. & Chen, L. Cancer associated fibroblasts:
899 An essential role in the tumor microenvironment. *Oncol. Lett.* **14**, 2611-2620
900 doi:10.3892/ol.2017.6497 (2017).
901 53 Sahai, E. *et al.* A framework for advancing our understanding of cancer-
902 associated fibroblasts. *Nat. Rev. Cancer* **20**, 174-186 doi:10.1038/s41568-019-
903 0238-1 (2020).
904 54 Johansson, A. C. *et al.* Cancer-associated fibroblasts induce matrix
905 metalloproteinase-mediated cetuximab resistance in head and neck squamous
906 cell carcinoma cells. *Mol. Cancer Res.* **10**, 1158-1168 doi:10.1158/1541-
907 7786.MCR-12-0030 (2012).
908 55 Rodriguez, A. B. *et al.* Immune mechanisms orchestrate tertiary lymphoid
909 structures in tumors via cancer-associated fibroblasts. *Cell Rep.* **36**, 109422
910 doi:10.1016/j.celrep.2021.109422 (2021).
911 56 Cabrita, R. *et al.* Tertiary lymphoid structures improve immunotherapy and
912 survival in melanoma. *Nature* **577**, 561-565 doi:10.1038/s41586-019-1914-8
913 (2020).
914 57 Helmink, B. A. *et al.* B cells and tertiary lymphoid structures promote
915 immunotherapy response. *Nature* **577**, 549-555 doi:10.1038/s41586-019-1922-8
916 (2020).
917 58 Fujii, N. *et al.* Cancer-associated fibroblasts and CD163-positive macrophages in
918 oral squamous cell carcinoma: their clinicopathological and prognostic

919 significance. *J. Oral Pathol. Med.* **41**, 444-451 doi:10.1111/j.1600-
920 0714.2012.01127.x (2012).
921 59 Gok Yavuz, B. *et al.* Cancer associated fibroblasts sculpt tumour
922 microenvironment by recruiting monocytes and inducing immunosuppressive PD-
923 1(+) TAMs. *Sci. Rep.* **9**, 3172 doi:10.1038/s41598-019-39553-z (2019).
924 60 Markwell, S. M. & Weed, S. A. Tumor and stromal-based contributions to head
925 and neck squamous cell carcinoma invasion. *Cancers (Basel)* **7**, 382-406
926 doi:10.3390/cancers7010382 (2015).
927 61 Munir, H. *et al.* Stromal-driven and Amyloid beta-dependent induction of
928 neutrophil extracellular traps modulates tumor growth. *Nat Commun* **12**, 683
929 doi:10.1038/s41467-021-20982-2 (2021).
930 62 Cong, X. *et al.* CD66b(+) neutrophils and alpha-SMA(+) fibroblasts predict clinical
931 outcomes and benefits from postoperative chemotherapy in gastric
932 adenocarcinoma. *Cancer Med* **9**, 2761-2773 doi:10.1002/cam4.2939 (2020).
933 63 Gaggioli, C. *et al.* Fibroblast-led collective invasion of carcinoma cells with
934 differing roles for RhoGTPases in leading and following cells. *Nat. Cell Biol.* **9**,
935 1392-1400 doi:10.1038/ncb1658 (2007).
936 64 Goetz, J. G. *et al.* Biomechanical remodeling of the microenvironment by stromal
937 caveolin-1 favors tumor invasion and metastasis. *Cell* **146**, 148-163
938 doi:10.1016/j.cell.2011.05.040 (2011).
939 65 Lin, J. R., Fallahi-Sichani, M. & Sorger, P. K. Highly multiplexed imaging of single
940 cells using a high-throughput cyclic immunofluorescence method. *Nat Commun*
941 **6**, 8390 doi:10.1038/ncomms9390 (2015).
942 66 Lin, J. R. *et al.* Highly multiplexed immunofluorescence imaging of human tissues
943 and tumors using t-CyCIF and conventional optical microscopes. *Elife* **7**
944 doi:10.7554/eLife.31657 (2018).
945 67 Virtanen, P. *et al.* SciPy 1.0: fundamental algorithms for scientific computing in
946 Python. *Nat. Methods* **17**, 261-272 doi:10.1038/s41592-019-0686-2 (2020).
947 68 Pedregosa, F. *et al.* Scikit-learn: Machine Learning in Python. *JMLR* **12**, 2825-
948 2830 (2011).
949 69 Seabold, S. & Perktold, J. statsmodels: Econometric and statistical modeling with
950 python. *Proceedings of the 9th Python in Science Conference* (2010).
951 70 Davidson-Pilon, C. *et al.* CamDavidsonPilon/lifelines: v0.21.0. *Zenodo*
952 doi:10.5281/zenodo.805993 (2020).
953

954 # TABLE LEGENDS

955 **Table 1. Patient and tumor characteristics.** Adapted from Banik et al[17] to show de-
956 identified patient characteristics.
957
958 **Table 2. mIHC cell phenotype classification.** Antibody panels used to hierarchically
959 phenotype cells into one of ten phenotype classifications. Additional functional markers
960 detected are listed at the bottom.
961
962 **Table 3. Coefficient of variation.** The coefficient of variation was calculated per tumor
963 per cell type and then averaged across all tumors (n=16). Tumors with only one region
964 (n=2) were removed from this analysis. Cell types are ordered from largest coefficient of
965 variation to smallest coefficient of variation.
966

967 # FIGURE LEGENDS

968 **Figure 1. Heterogeneity across patients and tumor regions. a**, Cohort and tissue
969 region selection overview. One to three regions of 2500^2 μm^2 were assayed with mIHC
970 per eighteen tumor resections and are represented by the green boxes in the tissue
971 images. The black line corresponds to 2500 μm for each image. **b**, Density (cells/mm^2)
972 of each cell type present per individual primary (P) and recurrent (R) tumor. Each dot
973 represents a single tumor region (n=47). **c**, Density (cells/mm^2) of each immune cell
974 type present per individual primary (P) and recurrent (R) tumor. Each dot represents a
975 single tumor region (n=47). **d**, Box plot of the Kullback-Leibler divergences from a single
976 tumor region's cellular distribution compared to: the tumor's average cellular distribution

977 [Intra-Tumor (P or R only)], the patient's average cellular distribution [Intra-Patient (P
978 and R)], the cohort's average cellular distribution across tumors of the same timepoint
979 [Inter-Patient (P or R only)], the cohort's average cellular distribution across tumors of
980 the same anatomic site [Inter-Patient (Same Anatomic Site)], the cohort's average
981 cellular distribution across all tumors from all patients [Inter-Patient (all)]. P-values
982 calculated using a one-way ANOVA multi-group significance test followed by a Tukey
983 honestly significant difference post-hoc test. **e**, Heatmap of cellular composition across
984 tumor regions. Rows are individual tumor regions that are ordered by the hierarchical
985 clustering of their cellular composition. Columns are the cell types used as clustering
986 features. Composition was normalized using a log10+1 transformation before clustering.
987 Leftmost three columns are color coded by patient, tumor timepoint, and anatomic site.
988 **f**, Principal component analysis on cellular density following a log10+1 transformation.
989 Each point (n=47) represents one tumor region and is colored by patient. The shape of
990 each point denotes primary or recurrent status. **g**, Principal component analysis on
991 cellular density following a log10+1 transformation. Each dot (n=47) represents one
992 tumor region and is colored by the anatomic resection site.
993
994 **Figure 2. Tumor cellular composition changes following therapy. a**, Box plot
995 showing the average density of each cell type split by primary and recurrent status.
996 Each dot represents the density of that cell type for one tumor, averaged across regions
997 (n=9 primary tumors, n=9 recurrent tumors). **b**, Line plots showing the change in cellular
998 composition from primary to recurrent tumors for each cell type. Each dot represents the
999 density of that cell type for one tumor, averaged across regions. Lines are colored by

1000 patient. **c**, Heatmap of average change in cellular composition from primary to recurrent
1001 tumors for each patient. Rows are individual patients that are ordered by the
1002 hierarchical clustering of their change in TiME cellular composition (averaged across
1003 regions). Columns are the cell types used as clustering features. Compositional change
1004 was normalized [-1,1] before clustering (see Methods). Leftmost two columns are color
1005 coded by patient followed by therapy administered. **d**, Box plot showing the average
1006 change in density of each cell type for each patient (n=9) colored by short-term or long-
1007 term progression free survival, splitting on median progression free survival.
1008
1009 **Figure 3. Mixing score quantifies the spatial organization of tumors. a**, mIHC
1010 images of a representative mixed tumor region (top) versus a compartmentalized tumor
1011 region (bottom). Leftmost panel shows tumor regions with neoplastic tumor cells
1012 (purple) and $CD45^+$ immune cells (green). Remaining panels show zoomed in areas of
1013 mixing (top) and compartmentalization (bottom), first with both cell populations present
1014 and then separated out. **b**, Box plot showing the mixing scores across all primary and
1015 recurrent tumors (n=18). Each dot (n=47) represents the mixing score for one tumor
1016 region and is colored according to its spatial architecture. The average spatial
1017 architecture designation for the overall tumor is printed above each box. **c**, Box plot
1018 showing the mixing score of each tumor region split by the anatomic site of its resection.
1019 P-value calculated using a one-way ANOVA multi-group significance test followed by a
1020 Tukey honestly significant difference post-hoc test. **d**, Kaplan-Meier curve of
1021 progression free survival for patients split by the mixing score of their primary tumors.
1022 Patients were split on the median value. P-value calculated using the log-rank test. **e**,

1023 Principal component analysis on cellular density following a log10+1 transformation.
1024 Each dot (n=47) represents one tumor region and is colored according to the region's
1025 spatial architecture. **f**, Box plot showing the density of each cell type split by the tumor
1026 region's spatial architecture. Each dot represents the density of that cell type for one
1027 region (n=47 per cell type). Statistical significance calculated using independent one-
1028 tailed t-tests for cell types whose differences follow a normal distribution and non-
1029 parametric one-tailed t-tests (Mann-Whitney U Test) for cell types whose differences do
1030 not follow a normal distribution. P-values were corrected using the Benjamini-Hochberg
1031 procedure. **g**, PD-1 expression on $CD8^+$ T cells, $CD4^+$ T helper cells, and B cells by
1032 spatial architecture. Each dot represents the percentage of each cell type positive for
1033 PD-1 for a single tumor region (n=45, excluding cold regions). P-values calculated using
1034 a one-tailed Mann-Whitney U test and corrected using the Benjamini-Hochberg
1035 procedure. **h**, Ki-67 expression on APCs by spatial architecture. Each dot represents
1036 the percentage of cells positive for Ki-67 for a single tumor region (n=45, excluding cold
1037 regions). P-values calculated using a Mann-Whitney U test and corrected using the
1038 Benjamini-Hochberg procedure. **i**, Bar chart showing the density of αSMA^+
1039 mesenchymal cells present per tumor region. Bars are ordered by αSMA^+ cell density
1040 and are colored according to the region's spatial architecture.
1041
1042 **Figure 4. αSMA^+ mesenchymal cellular neighborhood clustering**. **a**, Cellular
1043 neighborhoods were defined by drawing a circle of a specified radius around each seed
1044 cell (green) of a designated phenotype. Cells whose centers were inside the circle were
1045 considered neighbors of that seed cell. This figure was created using BioRender.com.

1046 **b**, Stacked bar chart showing the average cellular composition of each αSMA$^+$
1047 mesenchymal cell neighborhood cluster (n=7). Bars are colored by cell type and
1048 represent the average fraction (out of 1.0) of each cell type present in the
1049 neighborhoods belonging to each cluster. **c**, Heatmap of αSMA$^+$ cell neighborhood
1050 clusters present averaged across primary tumors. Rows are primary tumors that are
1051 ordered by the hierarchical clustering of their average of αSMA$^+$ neighborhood cluster
1052 presence. Columns are the αSMA$^+$ cell neighborhood clusters used as clustering
1053 features. Percent (out of 100) of αSMA$^+$ neighborhood clusters was normalized using a
1054 log10+1 transformation before clustering. Leftmost column is color coded by patient. **d**,
1055 Stacked bar chart showing the average proportion (out of 1.0) of αSMA$^+$ cell
1056 neighborhood clusters present in each of the two hierarchically clustered groups of
1057 primary tumors. **e**, Panel of mIHC images containing two merged pseudo-colored
1058 images of one region from 4 patients visually illustrates representative regions from
1059 patients in group 1 and group 2. The top panel of images are merged pseudo-colored
1060 stains containing CD3, CD8, CD20, αSMA, and PANCK. The bottom panel of images
1061 are the same regions as the top panel with merged pseudo-colored stains containing
1062 MHCII, CD66B, Ki-67, αSMA, and PANCK. White arrows point out representative
1063 αSMA$^+$ cells. **f**, Kaplan-Meier curve of progression free survival for patients grouped
1064 together in the hierarchical clustering of their primary tumor αSMA$^+$ mesenchymal cell
1065 neighborhood abundance. P-value calculated using the log-rank test. **g**, Stacked bar
1066 chart showing the average proportion (out of 1.0) of αSMA$^+$ cell neighborhood clusters
1067 present in each of the primary tumors (n=9). Tumors are ordered by descending
1068 proportions of cluster 1.

1069

1070 **Figure 5. Proposed model of primary HPV(-) HNSCC tumor-immune**
1071 **microenvironments. a**, Depiction of a tumor with a compartmentalized spatial
1072 architecture. These tumors have decreased mixing between immune cells and
1073 neoplastic tumor cells and tend to contain greater immune cell density, specifically
1074 those involved in antigen presentation, as well as increased density of αSMA^+
1075 mesenchymal cells. The αSMA^+ cells present tend to be neighbored by $CD4^+$ T helper
1076 cells and B cells, as well as other αSMA^+ cells. Compartmentalized primary tumors were
1077 found to be associated with longer progression free survival. **b**, Depiction of a tumor
1078 with a mixed spatial architecture. These tumors contain increased mixing between
1079 immune cells and neoplastic tumor cells and tend to contain increased neoplastic tumor
1080 cells, as well as increased PD-1-positive lymphocytes. The αSMA^+ cells present tend to
1081 be neighbored by neoplastic tumor cells, other immune cells, many of which are
1082 $CD163^+$ or are mast cells, and granulocytes. Mixed primary tumors were found to be
1083 associated with shorter progression free survival and later TNM stage. This figure was
1084 created using BioRender.com.

1085

1086 **Supplemental Figure 1a**. Gating template used to determine cell phenotypes and
1087 classification of ten populations using image gating cytometry in FCS Image Cytometry
1088 7 RUO. Scatter plots show single cell mean intensity distributions rescaled from 0-1 on
1089 a log10 scale with gated populations in colored boxes. Image plot shows a semi-
1090 transparent pseudo-colored mask of each cell object colored by the classified

population overlaid on signal extracted nuclei image. The markers used for identification of cell phenotypes are shown in Table 1.

Supplemental Figure 1b. mIHC images of six tumor regions selected from two different tumor resections (patient 9 primary and patient 8 recurrent). Blue pseudo color indicates all cell nuclei present in the region (Hematoxylin^{+}) and yellow indicates B cells. In both tumors, two regions have low densities of B cells, whereas one region has a high density and spatial concentration of B cells, despite the three regions being sampled from the same tumor.

Supplemental Figure 1c. Box plot of the Kullback-Leibler divergences from a single tumor region's immune cell distribution compared to: the tumor's average immune cell distribution [Intra-Tumor (P or R only)], the patient's average immune cell distribution [Intra-Patient (P and R)], the cohort's average immune cell distribution across tumors of the same timepoint [Inter-Patient (P or R only)], the cohort's average immune cell distribution across tumors of the same anatomic site [Inter-Patient (Same Anatomic Site)], the cohort's average immune cell distribution across all tumors from all patients [Inter-Patient (all)]. P-values calculated using a one-way ANOVA multi-group significance test followed by a Tukey honestly significant difference post-hoc test.

Supplemental Figure 2a. Box plot of the absolute difference from a single tumor region's mixing score compared to: the tumor's average mixing score [Intra-Tumor (P or R only)], the patient's average mixing score [Intra-Patient (P and R)], the cohort's

1114 average mixing score across tumors of the same timepoint [Inter-Patient (P or R only)],
1115 the cohort's average mixing score across tumors of the same anatomic site [Inter-
1116 Patient (Same Anatomic Site)], the cohort's average mixing score across all tumors
1117 from all patients [Inter-Patient (all)]. P-value calculated using a one-way ANOVA multi-
1118 group significance test.
1119
1120 **Supplemental Figure 2b**. Histogram showing the results of a bootstrapping analysis on
1121 the percentage of $CD8^+$ T cells expressing PD-1. Bars are colored by spatial
1122 architecture.
1123
1124 **Supplemental Figure 2c**. Histogram showing the results of a bootstrapping analysis on
1125 the percentage of $CD4^+$ T helper cells expressing PD-1. Bars are colored by spatial
1126 architecture.
1127
1128 **Supplemental Figure 2d**. Histogram showing the results of a bootstrapping analysis on
1129 the percentage of B cells expressing PD-1. Bars are colored by spatial architecture.
1130
1131 **Supplemental Figure 2e**. Histogram showing the results of a bootstrapping analysis on
1132 the percentage of APCs expressing Ki-67. Bars are colored by spatial architecture.
1133
1134 **Supplemental Figure 3a**. t-SNE representation of single cells from the 'Other Immune'
1135 class colored by heatmap of mean intensity for CD163 and tryptase (mast cells) show

1136 distinct populations of cells expressing high levels of CD163 and tryptase, indicating
1137 these cell types are likely present in the 'Other Immune' class.
1138
1139 **Supplemental Figure 3b**. Stacked bar chart showing the proportion (out of 1.0) of
1140 αSMA$^+$ cell neighborhood clusters present in each tumor region (n=47).
1141
1142 **Supplemental Figure 3c**. Stacked bar chart showing the average proportion (out of
1143 1.0) of αSMA$^+$ cell neighborhood clusters present in each tumor (n=18).
1144
1145 **Supplemental Figure 3d**. Stacked bar chart showing the proportion (out of 1.0) of
1146 αSMA$^+$ cell neighborhood clusters present in each patient's primary and recurrent
1147 tumors averaged (n=9).
1148
1149 **Supplemental Figure 3e**. Stacked bar chart showing the average proportion (out of
1150 1.0) of αSMA$^+$ cell neighborhood clusters present in tumors collected from the three
1151 anatomic sites.
1152
1153 **Supplemental Figure 3f**. Stacked bar chart showing the average proportion (out of 1.0)
1154 of αSMA$^+$ cell neighborhood clusters present in the primary tumors by their TNM stage.

Blise et al. Table 1

Patient ID	Anatomic Site of Resection	Primary Tumor TNM Stage	Therapy Following Primary Resection	Gender	Race	Alcohol History	Smoking History	HPV Status	Progression Free Survival (days)
1	Oral Cavity	2	Cisplatin + Radiation	Male	White	Yes	Yes	Negative	804
2	Oral Cavity	4	Cetuximab + Radiation	Male	White	Yes	Yes	Negative	123
3	Oral Cavity	1	Cisplatin + Radiation	Female	White	Yes	No	Negative	1447
4	Oral Cavity	1	Cisplatin + Radiation	Female	White	No	No	Negative	246
5	Oropharynx	4	Cetuximab + Radiation	Female	White	Yes	No	Negative	202
6	Oropharynx	4	Cisplatin + Radiation	Female	Asian	No	No	Negative	188
7	Larynx	4	Cisplatin + Cetuximab + Radiation	Female	White	Yes	Yes	Negative	409
8	Larynx	3	Cisplatin + Radiation	Female	White	Yes	Yes	Negative	1033
9	Larynx	4	Cisplatin + Radiation	Female	White	Yes	Yes	Negative	83

Cell Phenotype	Antibody Markers
$CD8^+$ T Cell	$CD45^+$ $CD20^-$ $CD3^+$ $CD8^+$
$CD4^+$ T Helper	$CD45^+$ $CD20^-$ $CD3^+$ $CD8^-$ $FOXP3^-$
$CD4^+$ Regulatory T Cell	$CD45^+$ $CD20^-$ $CD3^+$ $CD8^-$ $FOXP3^+$
B Cell	$CD45^+$ $CD20^+$
Macrophage	$CD45^+$ $CD20^-$ $CD3^-$ $CD66B^-$ $CD68^+$
Granulocyte	$CD45^+$ $CD20^-$ $CD3^-$ $CD66B^+$
Antigen Presenting Cell	$CD45^+$ $CD20^-$ $CD3^-$ $CD66B^-$ $CD68^-$ $MHCII^+$
Other Immune	$CD45^+$ $CD20^-$ $CD3^-$ $CD66B^-$ $CD68^-$ $MHCII^-$ $CD8^-$ $FOXP3^-$
αSMA^+ Mesenchymal	$CD45^-$ $PANCK^-$ αSMA^+
Neoplastic Tumor	$CD45^-$ $PANCK^+$
Additional Functional Markers: PD-1, PD-L1, Ki-67	

Cell Phenotype	Average Coefficient of Variation
B Cell	0.658
Macrophage	0.563
αSMA^+ Mesenchymal	0.545
Neoplastic Tumor	0.541
Granulocyte	0.523
Antigen Presenting Cell	0.519
Other Immune	0.402
$CD8^+$ T Cell	0.384
$CD4^+$ T Helper	0.376
$CD4^+$ Regulatory T Cell	0.311

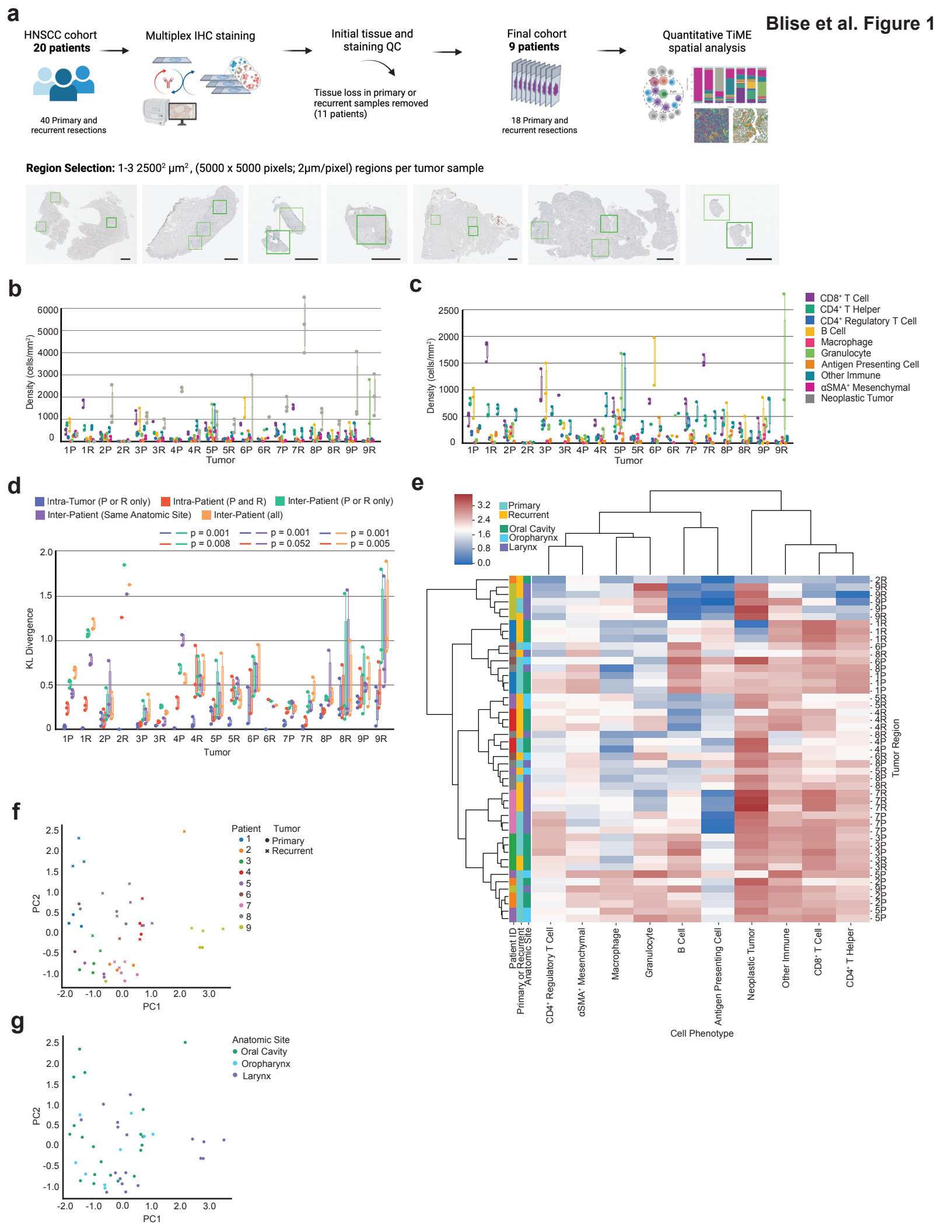

Blise et al. Figure 1
a
HNSCC cohort
20 patients
40 Primary and recurrent resections
Multiplex IHC staining
Initial tissue and staining QC
Tissue loss in primary or recurrent samples removed (11 patients)
Final cohort
9 patients
18 Primary and recurrent resections
Quantitative TiME spatial analysis
Region Selection: 1-3 2500² µm², (5000 x 5000 pixels; 2µm/pixel) regions per tumor sample
b
Density (cells/mm²)
Tumor
c
CD8⁺ T Cell
CD4⁺ T Helper
CD4⁺ Regulatory T Cell
B Cell
Macrophage
Granulocyte
Antigen Presenting Cell
Other Immune
αSMA⁺ Mesenchymal
Neoplastic Tumor
d
Intra-Tumor (P or R only)
Intra-Patient (P and R)
Inter-Patient (P or R only)
Inter-Patient (Same Anatomic Site)
Inter-Patient (all)
p = 0.001
p = 0.008
p = 0.001
p = 0.052
p = 0.001
p = 0.005
KL Divergence
Tumor
e
Primary
Recurrent
Oral Cavity
Oropharynx
Larynx
Tumor Region
Patient ID
Primary or Recurrent
Anatomic Site
CD4⁺ Regulatory T Cell
αSMA⁺ Mesenchymal
Macrophage
Granulocyte
B Cell
Antigen Presenting Cell
Neoplastic Tumor
Other Immune
CD8⁺ T Cell
CD4⁺ T Helper
Cell Phenotype
f
Patient
Tumor
Primary
Recurrent
PC1
PC2
g
Anatomic Site
Oral Cavity
Oropharynx
Larynx
PC1
PC2

Blise et al. Figure 2

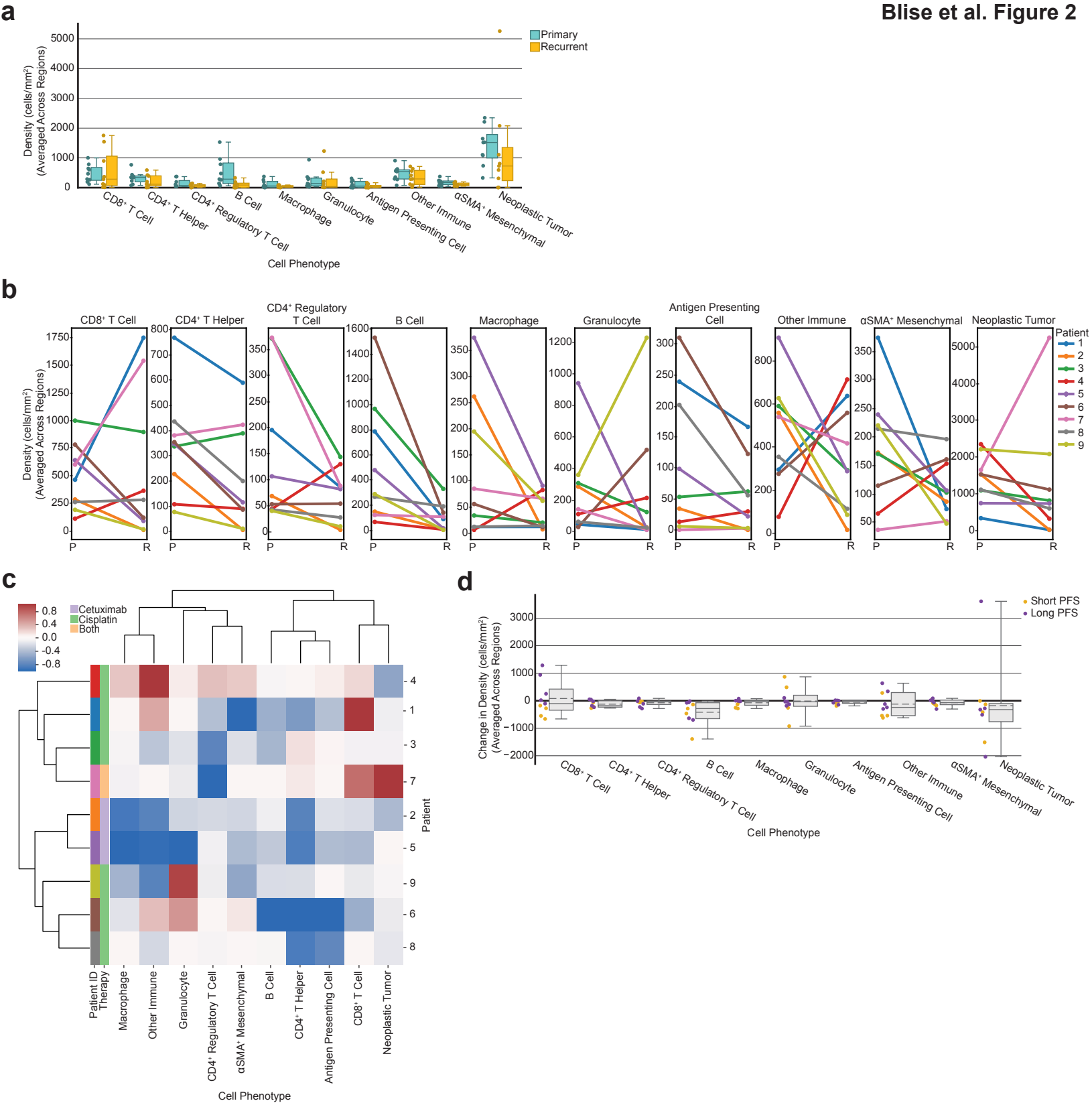

Blise et al. Figure 3

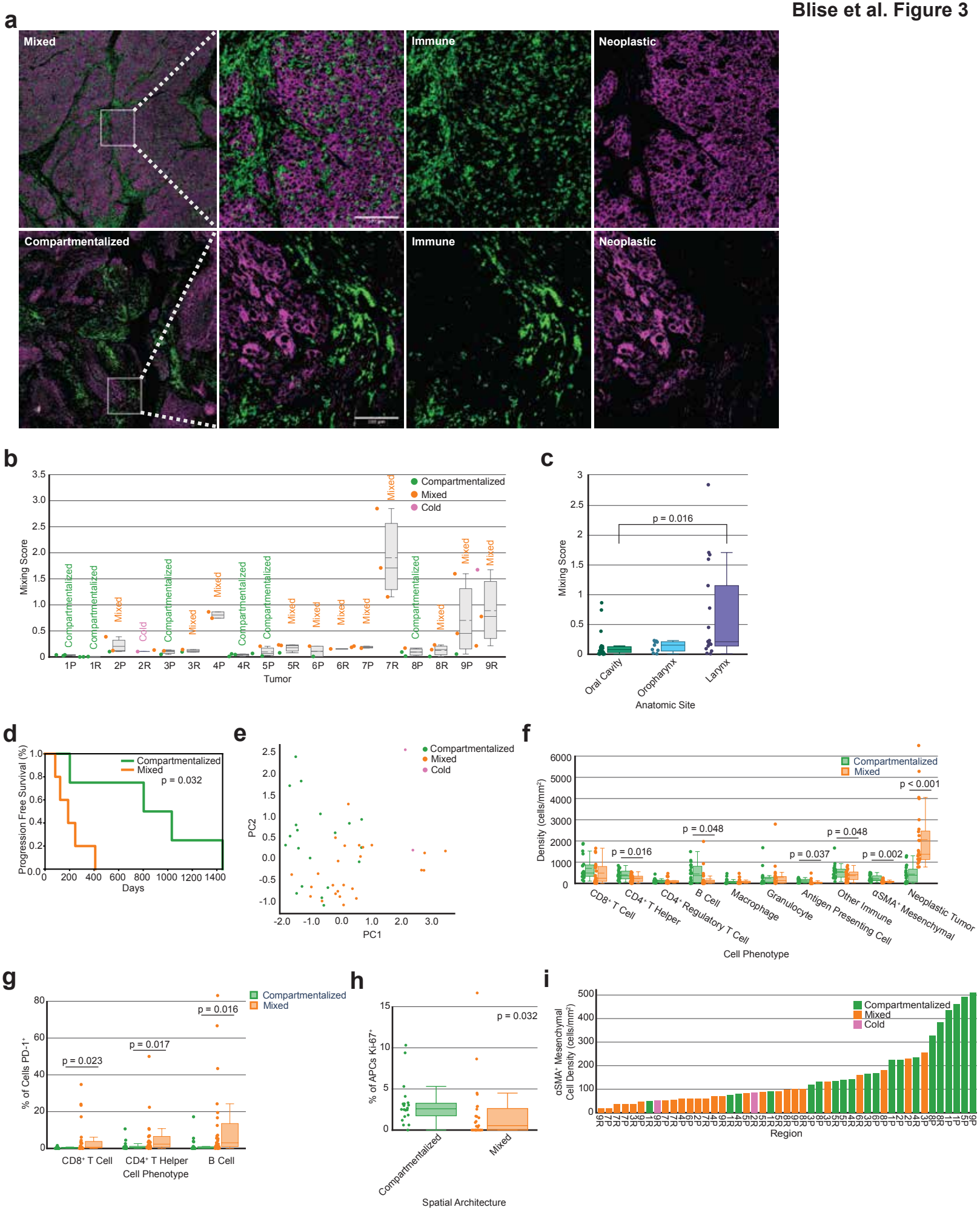

Blise et al. Figure 4

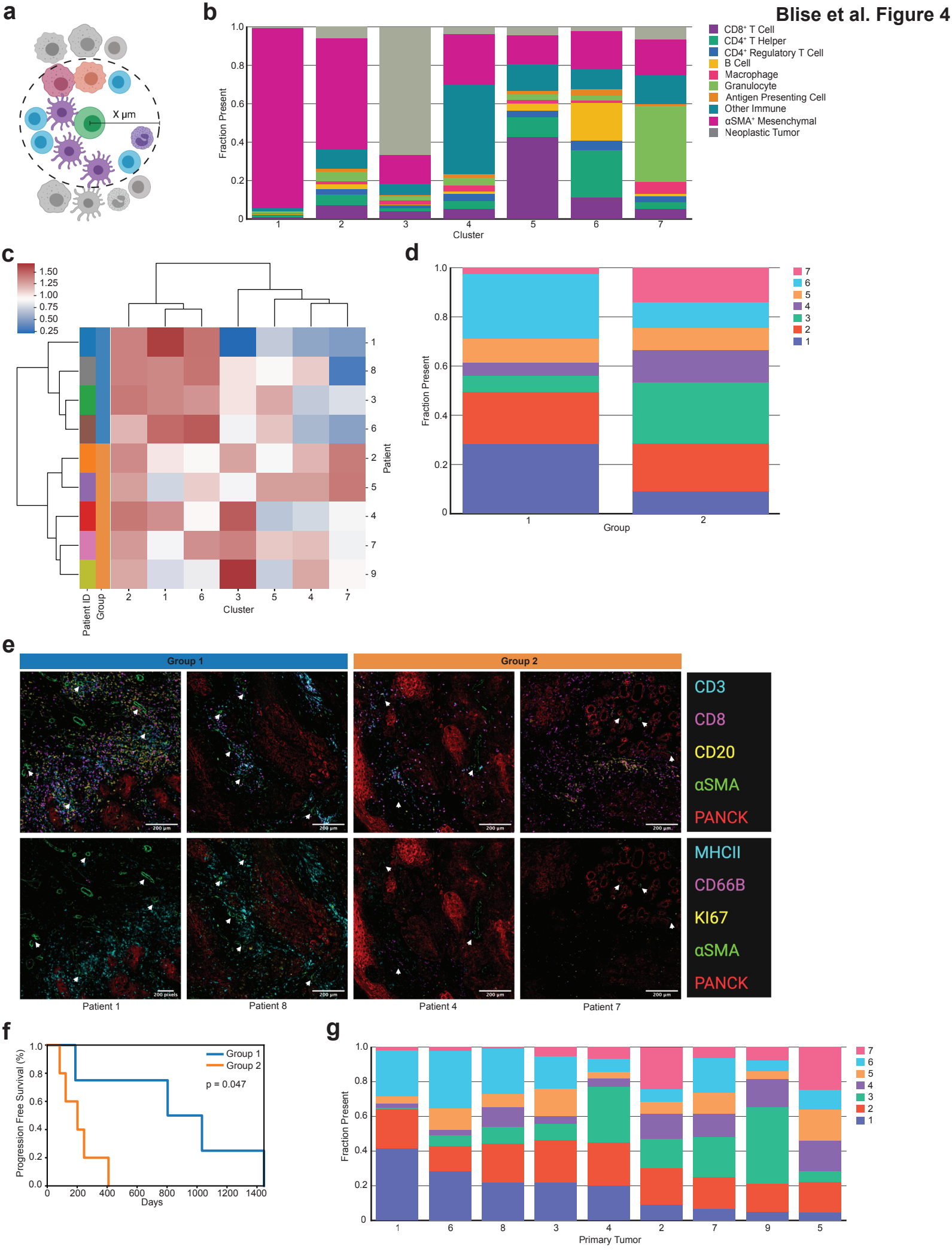

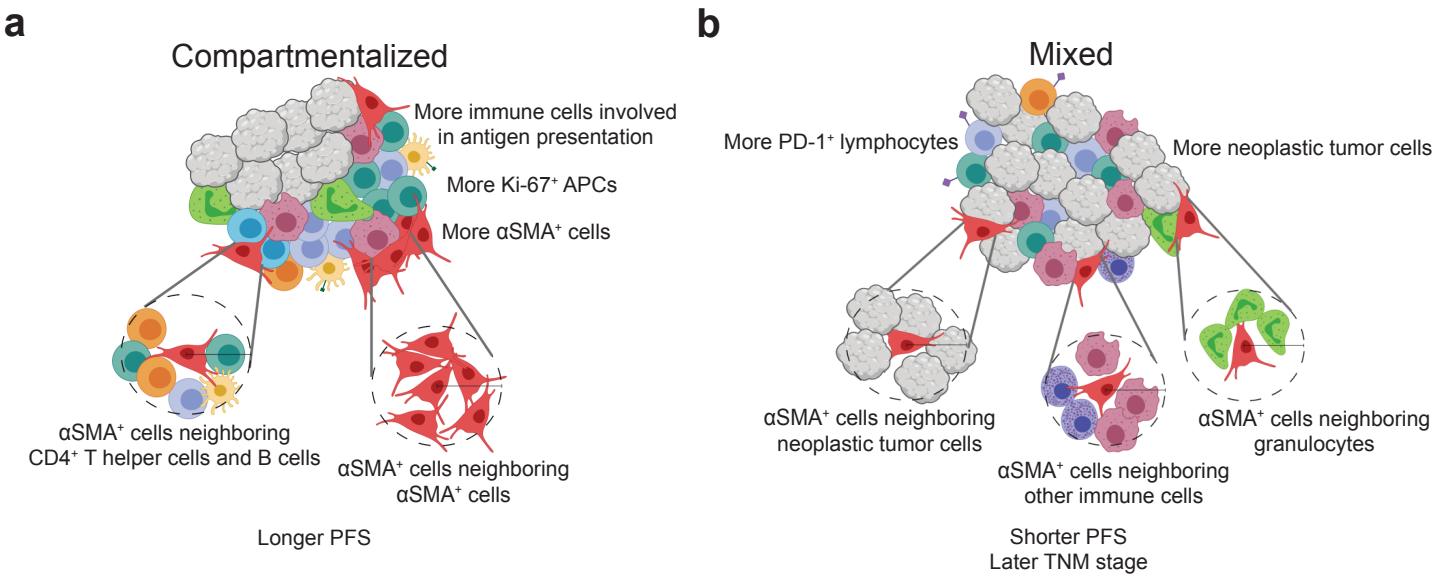
a
Compartmentalized
More immune cells involved in antigen presentation
More Ki-67+ APCs
More αSMA+ cells
αSMA+ cells neighboring CD4+ T helper cells and B cells
αSMA+ cells neighboring αSMA+ cells
Longer PFS
b
Mixed
More PD-1+ lymphocytes
More neoplastic tumor cells
αSMA+ cells neighboring neoplastic tumor cells
αSMA+ cells neighboring other immune cells
αSMA+ cells neighboring granulocytes
Shorter PFS
Later TNM stage

Blise et al. Supplemental Figure 1

a

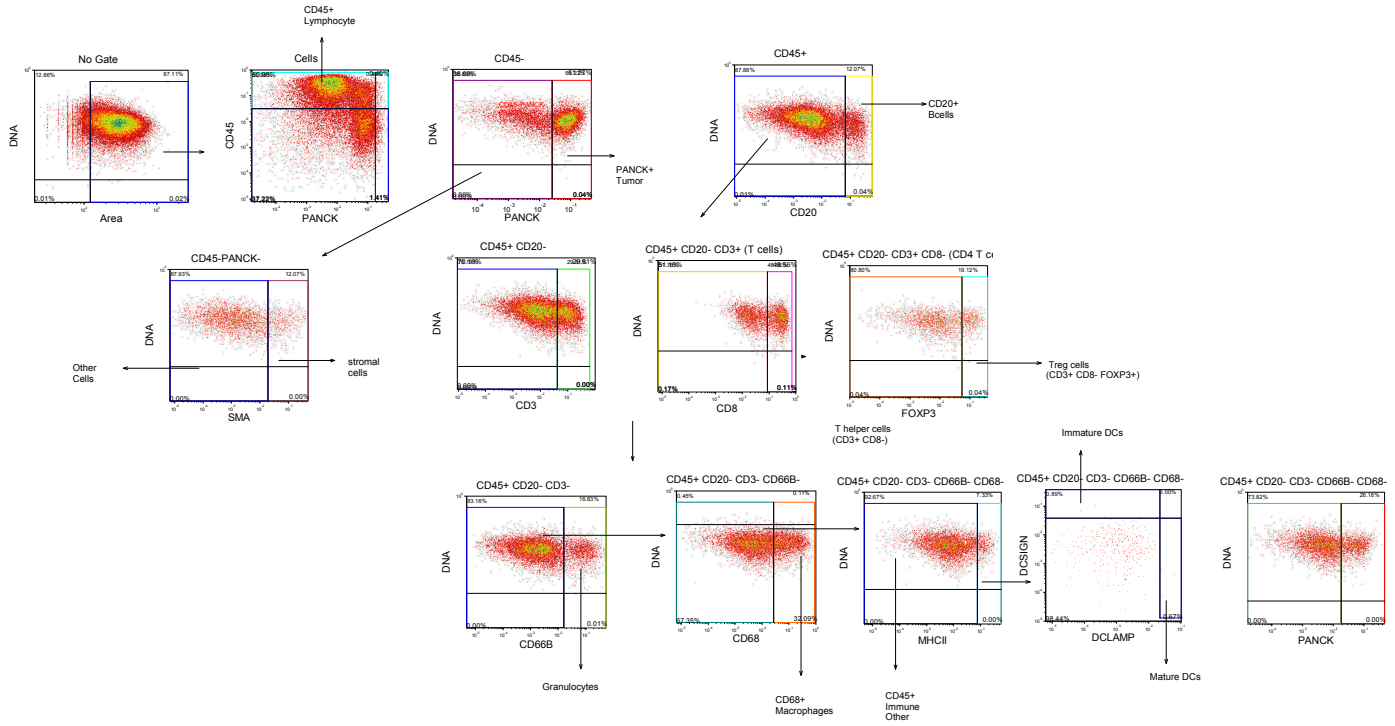

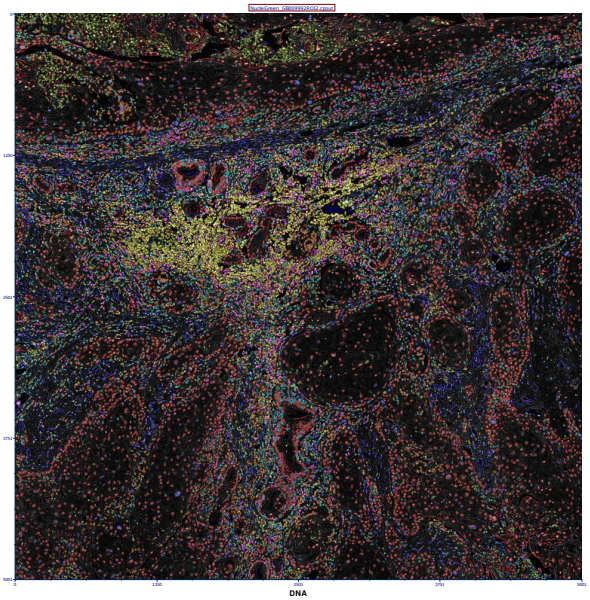

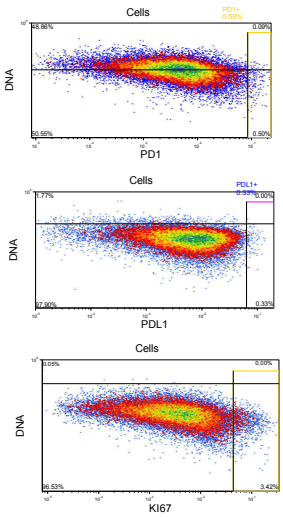

b

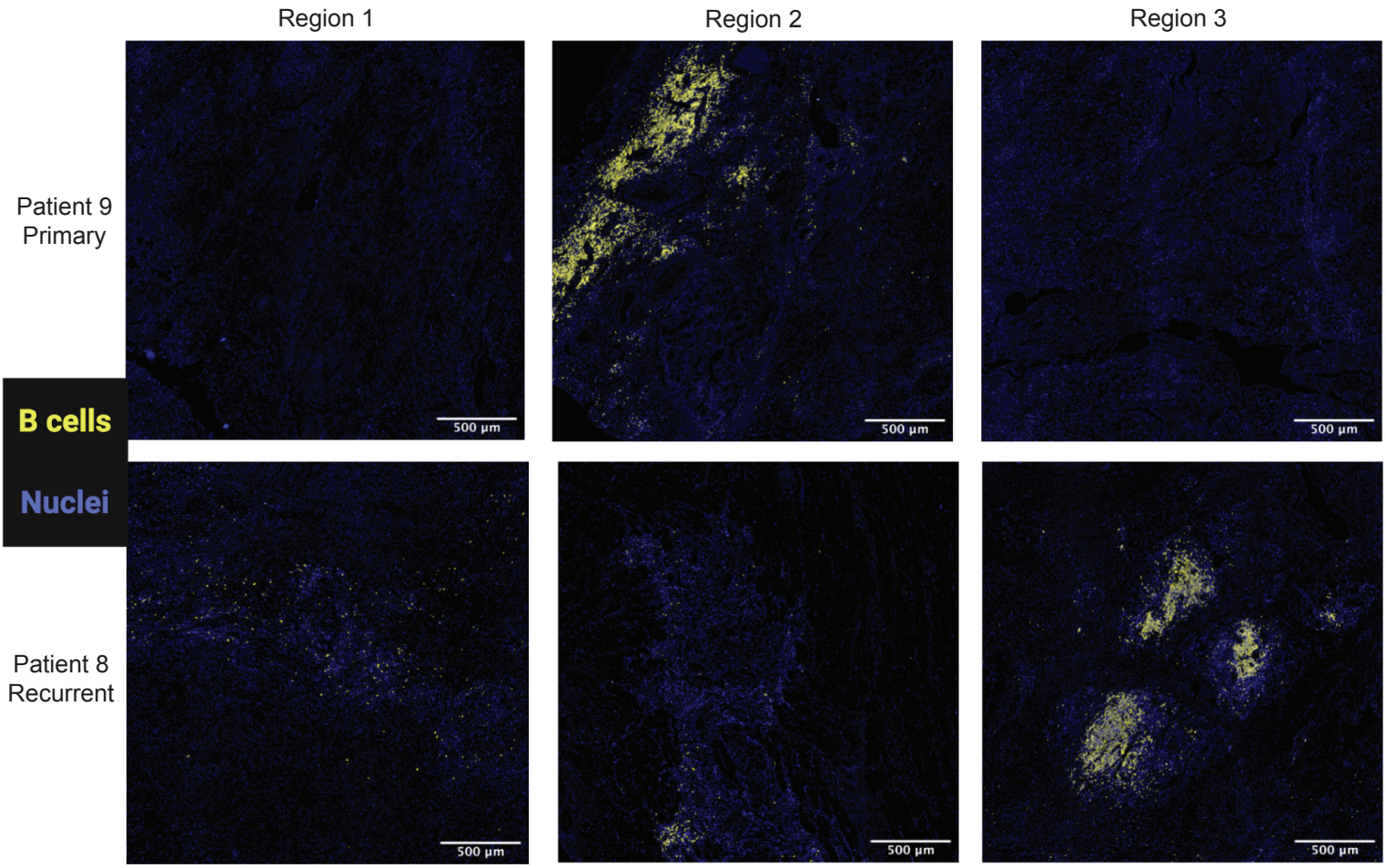
Region 1
Region 2
Region 3
Patient 9
Primary
B cells
Nuclei
Patient 8
Recurrent
500 µm

c

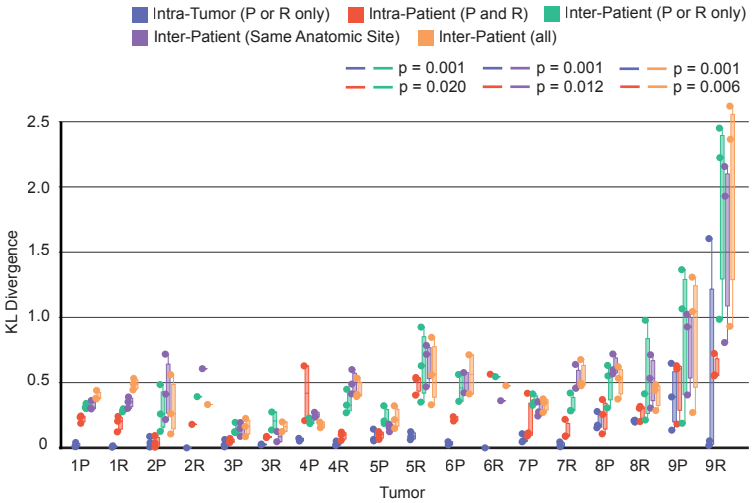
Intra-Tumor (P or R only)
Intra-Patient (P and R)
Inter-Patient (P or R only)
Inter-Patient (Same Anatomic Site)
Inter-Patient (all)
p = 0.001
p = 0.020
p = 0.001
p = 0.012
p = 0.001
p = 0.006
KL Divergence
0
0.5
1.0
1.5
2.0
2.5
1P 1R 2P 2R 3P 3R 4P 4R 5P 5R 6P 6R 7P 7R 8P 8R 9P 9R
Tumor

Blise et al. Supplemental Figure 2

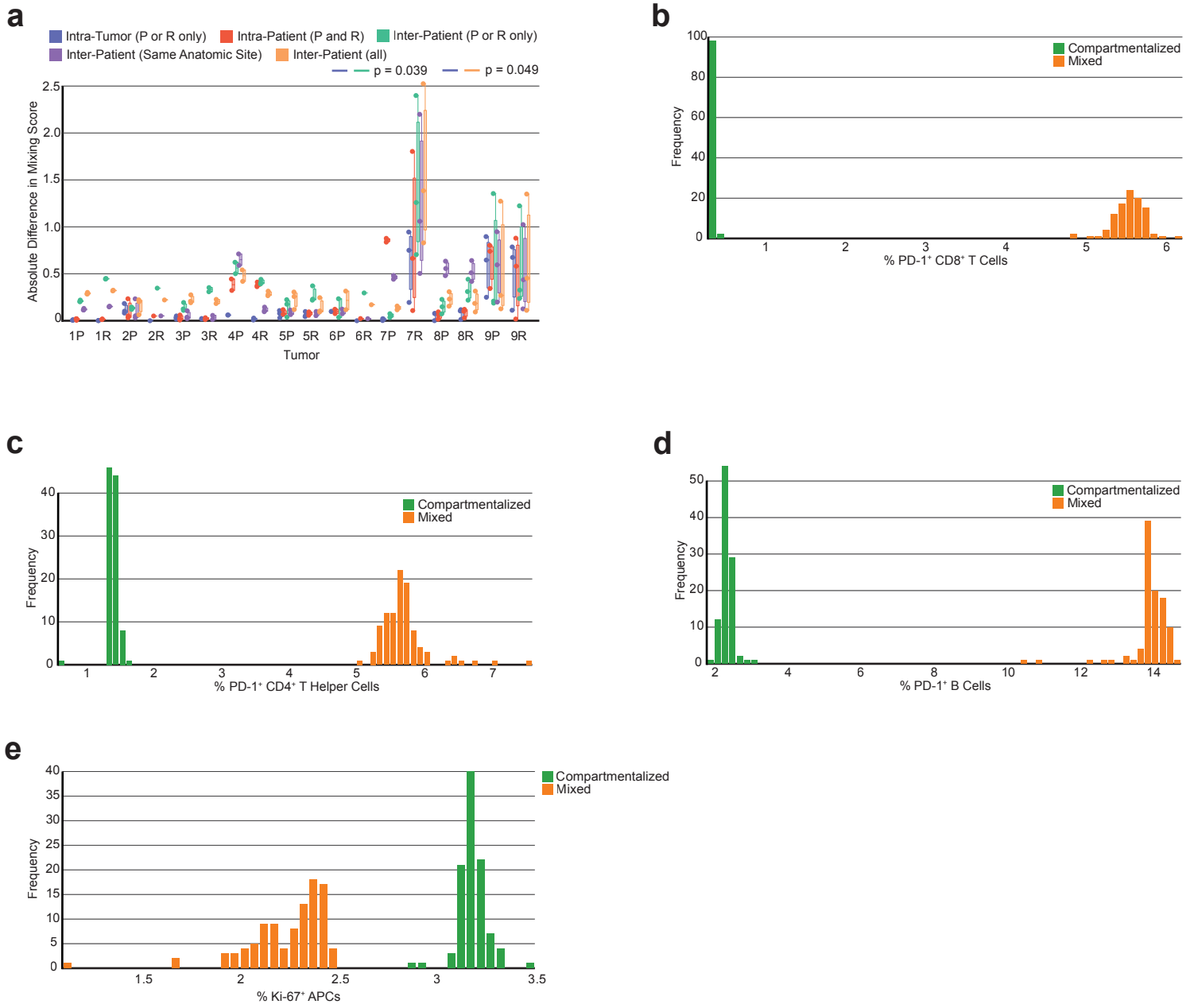
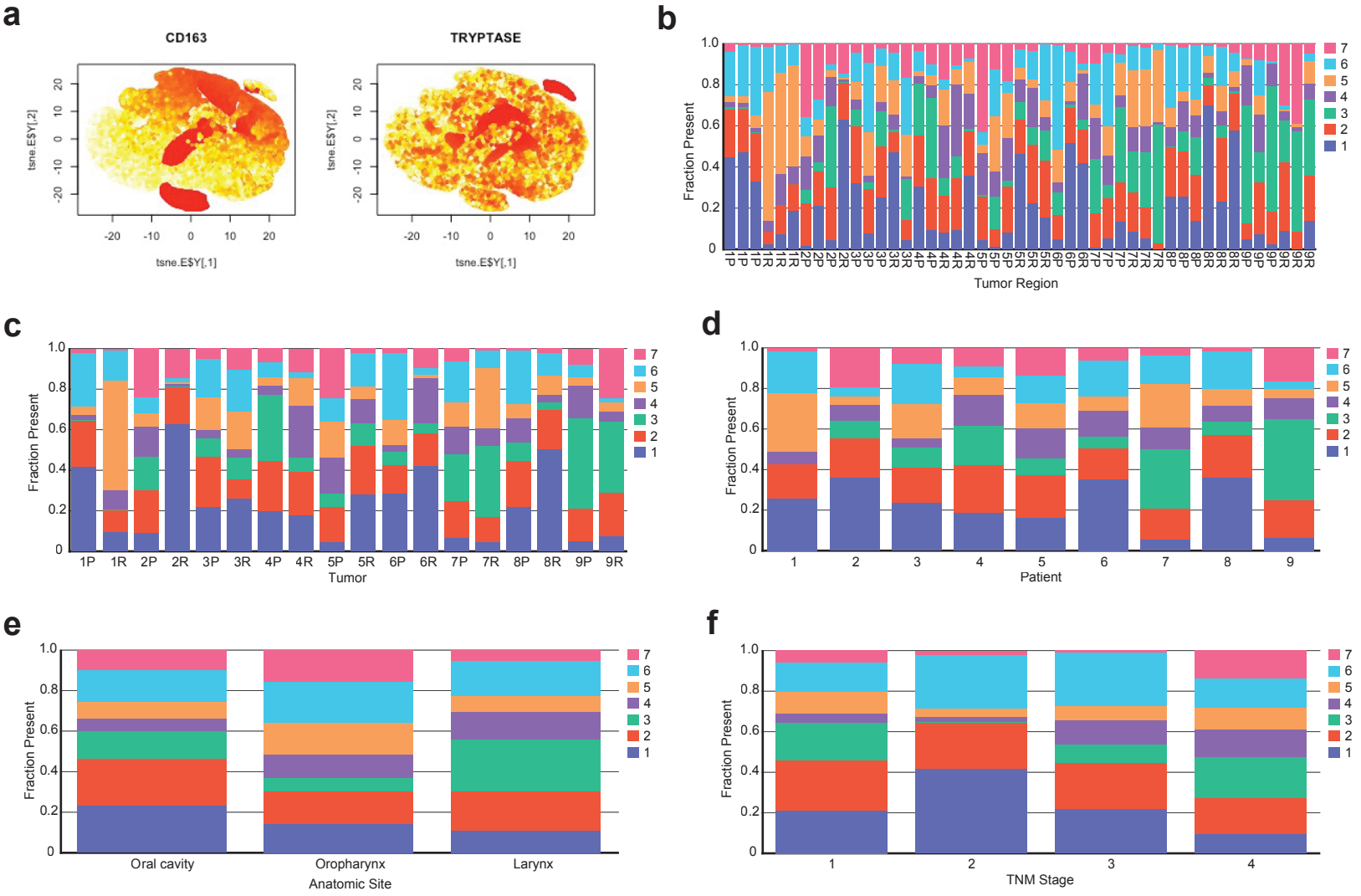
Blise et al. Supplemental Figure 3